A weakly non-hydrostatic shallow model for dry granular flows

J. Garres-Díaz [*], E.D. Fernández-Nieto [†], A. Mangeney [‡§], T. Morales de Luna[*]

Abstract

A non-hydrostatic depth-averaged model for dry granular flows is proposed, taking into account vertical acceleration. A variable friction coefficient based on the $\mu(I)$ rheology is considered. The model is obtained from an asymptotic analysis in a local reference system, where the non-hydrostatic contribution is supposed to be small compared to the hydrostatic one. The non-hydrostatic counterpart of the pressure may be written as the sum of two terms: one corresponding to the stress tensor and the other to the vertical acceleration. The model introduced here is weakly non-hydrostatic, in the sense that the non-hydrostatic contribution related to the stress tensor is not taken into account due to its complex implementation. The motivation is to propose simple models including non-hydrostatic effects. In order to approximate the resulting model, a simple and efficient numerical scheme is proposed. It consists of a three-step splitting procedure and the resulting scheme is well-balanced for granular material at rest with slope smaller than the fixed repose angle. The model and numerical scheme are validated by means of several numerical tests, including a convergence test, a well-balanced test, and comparisons with laboratory experiments of granular collapse. The influence of non-hydrostatic terms and of the choice of the coordinate system (Cartesian or local) is also analyzed. We show that non-hydrostatic models are less sensitive to the choice of the coordinate system. In addition, the non-hydrostatic Cartesian model produces deposits similar to the hydrostatic local model as suggested by Denlinger & Iverson [16], the flow dynamics being however different. Moreover, the proposed model, when written in Cartesian coordinates, can be seen as an improvement of their model, since the vertical velocity is computed and not estimated from the boundary conditions. In general, the non-hydrostatic model introduced here much better reproduces granular collapse experiments compared to hydrostatic models, especially at the beginning of the flow.

Keywords: Savage-Hutter model Non-hydrostatic pressure Finite Volume Granular flows.

Subclass: 35L60 76M1276T25 35L65.

[*]Dpto. Matemáticas. Edificio Einstein - Universidad de Córdoba. Campus de Rabanales, 14014-Córdoba, Spain, (jgarres@uco.es, tomas.morales@uco.es)

[†]Dpto. Matemática Aplicada I. ETS Arquitectura - Universidad de Sevilla. Avda. Reina Mercedes S/N, 41012-Sevilla, Spain, (edofer@us.es)

[‡]Institut de Physique du Globe de Paris, Seismology team, University Paris-Diderot, Sorbonne Paris Cité, 75238, Paris, France, (mangeney@ipgp.fr)

[§]ANGE team, CEREMA, INRIA, Lab. J. Louis Lions, 75252, Paris, France

1 Introduction

Granular flows have been intensely studied in recent years, since they play an important role in the understanding of natural hazards (avalanches, submarine landslides,...) and industrial processes. Aerial granular flow models as well as other more complex models such as debris flows have been widely studied (e.g. [30, 46, 28, 5]) and applied to simulate laboratory experiments [38, 29] and real landslides [33, 45, 35] up to hazard assessment [42, 44]. The physical description of these type of flows is a very active field of research from several points of view. On the one hand, the definition of rheological laws describing the complex dynamics of the flow is a challenge nowadays [1, 14], namely the solid-fluid transition occurring when a granular material is flowing. On the other hand, the mathematical modelling of these flows is a difficult issue, since the stress tensor has a complex expression usually, and therefore its numerical treatment is not straightforward.

From the physical point of view, the $\mu(I)$ rheology, introduced in Jop, Forterre & Pouliquen [31, 32], is the most accepted rheological law describing dry granular flows. It considers a pressure and strain-rate dependent viscosity, through a variable friction coefficient depending on the inertial number. In addition, in recent years, some works have been devoted to improving this law by adding non-local effects to the $\mu(I)$ rheology. However, there are still many open questions around these non-local models (see e.g. [50, 8]). Thus, the local $\mu(I)$ rheology continues being a very popular law for physicist when describing dry granular flows and start to be used for landslide simulation at the field scale [10].

The $\mu(I)$-rheology was implemented in a 2D continuous model solving the full Navier-Stokes equations by Staron, Lagrée & Popinet [52] by using a regularization method to describe the static behavior of the material. By fitting the rheological parameters of the $\mu(I)$-rheology down to values smaller that those of the granular material involved, they were able to reproduce 2D discrete elements simulations. Ionescu *et al.* [27] and Martin *et al.* [40] quantitatively reproduced laboratory experiments of a granular collapse problem using finite element discretizations of the full 2D equations and an Augmented Lagrangian method, as well as a simplified description of the lateral wall effects. Bouchut *et al.* [6] derived an analytic expression for the non-hydrostatic pressure. It is based on an asymptotic analysis under some hypothesis, such as shallow flow and small velocity. As a consequence, only the terms related to the stress tensor are considered in the definition of the non-hydrostatic pressure counterpart, while the acceleration in the direction normal to the slope is neglected. This analytical formulation of the pressure is compared with the pressure computed solving the full 2D Navier-Stokes equations, showing that these non-hydrostatic analytical terms describe well part of the non-hydrostatic pressure (see Figure 18 of [40]), although the effect of the vertical acceleration is not taken into account.

It is a well-known fact that the computational cost of solving flows with a moving free surface with a 3D (or 2D) solver is huge. Shallow depth-averaged and hydrostatic layer-averaged models have been widely used in order to reduce this computational effort. These models are mainly based on the pioneering work of Savage-Hutter [51], where the friction between the bottom and the granular material is modelled though a constant Coulomb friction coefficient. Pouliquen [48, 47] proposed to replace this constant value by a friction coefficient depending on the strain rate. In a more recent work, Pouliquen & Forterre [49] proposed to make this coefficient depend on the Froude number. The resulting model was used by Mangeney-Castelnau *et al.* [39] and Mangeney *et al.* [36] to simulate granular flows on simple topography, making it possible to reproduce qualitatively self-channeling flows and levee formation. It has also been successfully used to simulate real landslides over complex topography (e. g. [45, 10]). More recently, Gray & Edwards [26] proposed a slightly modified depth-averaged model by including second-order viscous terms derived by assuming a Bagnold profile for the downslope velocity.

It reduced to the model of [48] when these second-order terms are dropped. This model, combined with the friction coefficient proposed by [49], is used in Edwards & Gray [17] to simulate roll-waves and erosion-deposition waves and in Baker *et al.* [3], making it possible to recover the transversal profile of the downslope velocity. However, the main drawback of this model is the fact that the velocity profile is prescribed even though the shape of the velocity profile is known to change during the flow. This change can be handled using multilayer models as done by Fernández-Nieto *et al.* [22, 23] that also used the $\mu(I)$ rheology. Indeed such models have been shown to reproduce the observed change in velocity profiles during granular flows on inclined planes. Using multilayer models, [22] also showed that the $\mu(I)$ rheology better reproduces the dynamics of granular flows than using a constant friction coefficient.

In all these depth-averaged or multilayer models, the pressure is assumed to be hydrostatic. In addition, as explained before, the analytic formula for the pressure proposed by [6] includes the rheology terms but not the normal acceleration terms due to their assumption of small velocity flows. Furthermore, it is well known that the initial dynamics of granular collapse is not well reproduced by shallow depth-averaged models, in particular because of the importance of non-hydrostatic effects in this regime (e. g. [38], [22, 23]). Therefore, a non-hydrostatic shallow model for granular flows, which takes into account the acceleration in the direction normal to the slope may significantly improve the ability of depth-averaged models to reproduce flow regimes where non-hydrostatic effects are important such as during the first instant of granular collapses.

Non-hydrostatic shallow water models have been a popular topic of research in recent years. The idea is to improve nonlinear dispersive properties of water waves by including some information on the vertical structure of the model. One way of doing so is by including a non-hydrostatic pressure in the model. In the usual process of averaging the fully 3D equations, the pressure is no longer assumed to be hydrostatic and is split into a hydrostatic and a non-hydrostatic part (see for instance [13], [53], [9], and [54], among others). The advantage of non-hydrostatic models when compared to classical dispersive systems is that they present only first-order derivatives, which are easier to treat numerically (see e.g. [19]). Moreover, the particular structure of these type of models and their similarities with shallow water equations allow extending many well-known numerical schemes for shallow water equations to non-hydrostatic models, see for instance [18]. In view of the improvement and possibilities of this technique for shallow waters, one could think that a similar approach would be interesting for granular flows.

The choice of the coordinate system plays a key role, in particular in depth-averaged models, which are obtained after an integration procedure. If a Cartesian coordinate system is chosen, the 3D model is integrated along the vertical Cartesian direction. However, it is usual in geophysical flows to use local coordinates (see e.g. [45, 26, 5]), where the integration is made along the normal direction to the topography, typically a reference plane with constant slope (although it may vary along the domain [20]) or an arbitrary topography [7, 36] where curvature effects may strongly impact the flow dynamics and deposit [43]. These models are more accurate for granular flows since the computed velocity is tangent to the topography, which is physically relevant, in contrast to Cartesian models. Recently, Delgado-Sánchez *et al.* [15] proposed a two-layer depth-averaged model, where they use Cartesian coordinates for an upper water layer and local coordinates for a lower granular layer since for water waves the vertical acceleration can be supposed to be small while for granular flows the acceleration normal to the slope is small. They showed that large errors are obtained when the coordinate system is not correctly chosen. Denlinger & Iverson [16] proposed a Cartesian model for landslides, where the pressure is corrected by an approximation of the vertical acceleration. They show that the results of this Cartesian model are close to the results of a hydrostatic model in local coordinates for dam break analytical solutions. In this model, the vertical acceleration is introduced in the approximate non-hydrostatic pressure by

taking the average between the vertical velocity derived from the free surface and bottom boundary conditions. As a result, the vertical velocity is not computed as an unknown of the system.

In this paper we deduce a simple model for granular flows including non-hydrostatic effects related to the acceleration in the direction normal to the slope. Then, a simple and efficient numerical scheme will be proposed that will allow us to notably improve the results of hydrostatic models. To our knowledge, this is the first non-hydrostatic shallow model (computing the normal acceleration) for dry granular flows. It follows from an asymptotic analysis and the decomposition of the pressure into a hydrostatic pressure and a small perturbation (non-hydrostatic contribution). For simplicity, the non-hydrostatic pressure will be assumed to follow a linear profile in the normal direction. Note that this is a simplification so that the final system is easier to deal with. Nevertheless, other type of profiles could be used, which would result in a more complex model, including extra variables and equations (see for instance the approaches used in [24, 19]). The model will take into account a bottom friction coefficient defined by the $\mu(I)$ rheology. Although the model will be derived using local coordinates, one may follow easily the same procedure in order to obtain a similar version in Cartesian coordinates. In [16], a Cartesian non-hydrostatic model is also proposed. The main differences are: (i) in the proposed model the vertical velocity is an unknown, whereas in [16] it is estimated in terms of the kinematic boundary conditions; (ii) the non-hydrostatic pressure correction in the proposed model is the Lagrange multiplier associated to averaged incompressibility equation, while in [16] it is approximated from the total time derivative of the estimated vertical velocity.

This paper is organised as follows. In Section 2 we present the initial system and the derivation of the non-hydrostatic model, based on an asymptotic analysis. Section 3 is devoted to the development of an efficient numerical scheme to approximate the proposed non-hydrostatic model. This is done with a three-step splitting technique, where the friction term is applied before solving the non-hydrostatic pressure. This is one of the key points of the scheme. In Section 4 different numerical tests are presented, including convergence and well-balance tests. An objective is to show the influence of the choice of the coordinate system (Cartesian or local) for hydrostatic and non-hydrostatic models. We also present a comparison with experimental data of granular collapses over inclined planes, showing that the non-hydrostatic model gives better results than the hydrostatic one, especially at short times and more generally on the mass profiles during the spreading up to the deposit. In addition, non-hydrostatic models make it possible to include the vertical velocity as a variable in the model and thus to simulate the effect of the opening gate in the laboratory experiments, which is not possible with hydrostatic model. Finally, some conclusions are presented in section 5.

2 Derivation of a non-hydrostatic shallow $\mu(I)$-model

In this section we deduce the non-hydrostatic model. It follows from an asymptotic analysis of the 2D Navier-Stokes system and the integration of the resulting equations along the normal direction to the topography.

2.1 Initial system

First, let us establish the notation used in this paper. In particular, we shall consider two different reference systems. We shall use local (or tilted) coordinates, as is usually done in granular flows, as well as Cartesian coordinates. We shall denote by (x, z) the Cartesian coordinate system (the flow is assumed to be independent of the y-direction), while (X, Z) will denote the local coordinates. This local coordinates will refer to a given fixed inclined plane (being a straight line in the $x - z$ plane).

More explicitly, let us consider an inclined reference plane with slope θ, that is a plane given by the function $\widetilde{b}(x) = (x_{end} - x)\tan\theta$, where x_{end} is the ending point of the domain. Let us remark that we consider here the usual convention in geophysical applications which establishes that a positive angle θ corresponds to a negative slope. Local coordinates (X, Z) are then considered, measured along the downslope and normal direction to the reference plane, $\widetilde{b}(x)$, respectively. The velocity vector is $\boldsymbol{u} = (u, w)$, where u is the downslope component of the velocity and w is the normal one. Finally, we consider also a bottom topography $b(X)$ over the reference inclined plane (see Figure 1).

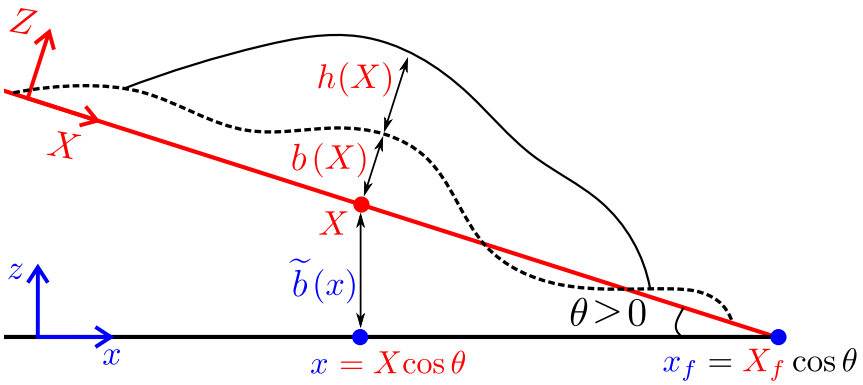

Figure 1: Sketch of the Cartesian (blue) and local (red) reference system.

As starting point, we consider the 2D Navier-Stokes system for a flow with constant density ρ given by

$$\begin{cases} \partial_X u + \partial_Z w = 0, \\ \partial_t u + u\,\partial_X u + w\,\partial_Z u + \dfrac{1}{\rho}\partial_X(p_T) = g\sin\theta + \dfrac{1}{\rho}\big(\partial_X(\tau_{XX}) + \partial_Z(\tau_{XZ})\big), \\ \partial_t w + u\,\partial_X w + w\,\partial_Z w + \dfrac{1}{\rho}\partial_Z(p_T) = -g\cos\theta + \dfrac{1}{\rho}\big(\partial_X(\tau_{ZX}) + \partial_Z(\tau_{ZZ})\big), \end{cases} \tag{1}$$

where g is the gravity force, p_T is the total pressure and

$$\boldsymbol{\tau} = \begin{pmatrix} \tau_{XX} & \tau_{XZ} \\ \tau_{ZX} & \tau_{ZZ} \end{pmatrix}$$

is the deviatoric part of the total stress tensor, $\boldsymbol{\sigma} = -p_T\mathbf{I} + \boldsymbol{\tau}$, where $\mathbf{I}$ is the identity matrix.

The total pressure shall be decomposed as sum of the hydrostatic and the non-hydrostatic contribution (see e.g. Casulli [13])

$$p_T = p_H + p_{NH}, \tag{2}$$

where $p_H = g\cos\theta\,(b + h - z)$ is the hydrostatic pressure and p_{NH} denotes the non-hydrostatic counterpart. The atmospheric pressure has been set to zero for the sake of simplicity and we shall assume that the non-hydrostatic pressure vanishes at the surface

$$p_{NH|_{b+h}} = p_{H|_{b+h}} = p_{T|_{b+h}} = 0.$$

We also assume that $\tau_{XZ_{|b+h}} = 0$. We consider at the free surface the usual kinematic condition

$$\partial_t h + u_{|b+h}\partial_X b - w_{|b+h} = 0. \tag{3}$$

At the bottom, we have the non-penetration condition

$$\boldsymbol{u} \cdot \mathbf{n}^b = 0, \tag{4}$$

where $\mathbf{n}^b = (\partial_X b, -1)$ is the downward normal vector to the bottom.

In addition, a Coulomb-type friction condition is considered:

$$\boldsymbol{\sigma}\ \boldsymbol{n}^b - \left(\left(\boldsymbol{\sigma}\ \boldsymbol{n}^b\right) \cdot \boldsymbol{n}^b\right) \boldsymbol{n}^b = \left(-\mu\, p_T \frac{u}{|u|},\ 0\right)', \tag{5}$$

where the prime ($'$) denotes the transposed vector, and here μ denotes the friction coefficient. This coefficient may be constant (i.e., Savage-Hutter model [51]) or variable according to some other rheological laws [35, 14]. Currently, the $\mu(I)$ rheology (see e.g. [31]) is the most accepted law describing dry granular flows. Therefore, we shall consider this rheology and define

$$\mu = \mu(I) = \mu_s + \frac{\mu_2 - \mu_s}{I_0 + I}\, I, \tag{6}$$

where μ_s, μ_2, I_0 are constant values, and I is the inertial number defined as

$$I = \frac{2d_s \|D(\boldsymbol{u})\|}{\sqrt{p_T/\rho_s}}.$$

In the previous equation, d_s is the particle diameter, ρ_s the particle density, and $D(\boldsymbol{u})$ is the strain-rate tensor with $\|D(\boldsymbol{u})\| = \sqrt{0.5 D : D}$. Note that the apparent flow density is $\rho = \rho_s \varphi_s$, where φ_s is the solid volume fraction. This rheological law is included in system (1) by defining the deviatoric stress tensor $\boldsymbol{\tau} = \nu D(\boldsymbol{u})$, where the viscosity coefficient, ν, is defined according to the $\mu(I)$ rheology as (see e.g. [34, 22])

$$\nu = \frac{\mu(I) p_T}{\|D(\boldsymbol{u})\|}. \tag{7}$$

2.2 Dimensional analysis and derivation of the model

We follow a classical dimensional analysis for dry granular flows (see e.g. [26, 23]) to obtain a simplified shallow model. Therefore, the ratio between the characteristic height (H) and length (L) is assumed to be small

$$\varepsilon = \frac{H}{L}.$$

We denote as well by U the characteristic velocity. In what follows, we will denote with tildes ($\widetilde{\cdot}$) the non-dimensional variables. Then, we have:

$$(X, Z, t) = (L\widetilde{X}, H\widetilde{Z}, (L/U)\widetilde{t}),$$

$$(u, w) = (U\widetilde{u}, \varepsilon U \widetilde{w}),$$

$$h = H\widetilde{h}, \quad \rho = \rho_0 \widetilde{\rho}, \quad p_T = \rho_0 U^2 \widetilde{p_T},$$

$$(\tau_{XX}, \tau_{XZ}, \tau_{ZZ}) = \rho_0 U^2 \left(\varepsilon\widetilde{\tau_{XX}}, \widetilde{\tau_{XZ}}, \varepsilon\widetilde{\tau_{ZZ}}\right).$$

Note also that

$$D(\boldsymbol{u}) = \frac{U}{H}\,\frac{1}{2}\begin{pmatrix} 2\varepsilon\partial_{\widetilde{X}}\widetilde{u} & \partial_{\widetilde{Z}}\widetilde{u} + \varepsilon^2\partial_{\widetilde{X}}\widetilde{w} \\ \partial_{\widetilde{Z}}\widetilde{u} + \varepsilon^2\partial_{\widetilde{X}}\widetilde{w} & 2\varepsilon\partial_{\widetilde{Z}}\widetilde{w} \end{pmatrix}, \quad \text{and} \quad \|D(\boldsymbol{u})\| = |\partial_Z u|/2$$

up to first order. Defining now the Froude number as $Fr = U/\sqrt{gH\cos\theta}$ and dropping tildes for the sake of simplicity, system (1) is written in non-dimensional form as

$$\begin{cases} \partial_X u + \partial_Z w = 0, & \text{(8a)} \\ \rho\big(\partial_t u + u\partial_X u + w\partial_Z u\big) + \partial_X(p_T) = \dfrac{1}{\varepsilon}\dfrac{\rho}{Fr^2}\tan\theta + \varepsilon\partial_X(\tau_{XX}) + \dfrac{1}{\varepsilon}\partial_Z(\tau_{XZ}), & \text{(8b)} \\ \rho\varepsilon^2\big(\partial_t w + u\partial_X w + w\partial_Z w\big) + \partial_Z(p_T) = -\dfrac{\rho}{Fr^2} + \varepsilon\partial_X(\tau_{ZX}) + \varepsilon\partial_Z(\tau_{ZZ}). & \text{(8c)} \end{cases}$$

Note that the deviatoric tensor is multivalued and we only know that $|\boldsymbol{\tau}_{XZ}| \leq \mu(I)p_T$ if $|D| = 0$ (see e.g. [27]).

The friction condition (5) at the bottom is given by

$$(\tau_{XZ},\ 0)' = \left(\mu(I)p_T\frac{u}{|u|},\ 0\right)' \quad \text{if } |u| \neq 0, \qquad \text{at } z = b, \tag{9}$$

while this friction condition is multivalued if $|u| = 0$, where $\left|\boldsymbol{\tau}_{XZ|_b}\right| \leq \mu(I_{|_b})p_{T|_b}$ in this case.

Finally, we assume that the non-hydrostatic pressure is smaller than the hydrostatic one. To this aim, we consider that the pressure takes the form

$$p_T = p_H + \varepsilon q_1 + \varepsilon^2 q = \frac{\rho}{Fr^2}(b + h - z) + \varepsilon q_1 + \varepsilon^2 q,$$

where q_1, q are the first and second order terms of the non-hydrostatic counterpart. It leads to the vertical momentum conservation equation

$$\rho\varepsilon^2\big(\partial_t w + u\,\partial_X w + w\,\partial_Z w\big) + \varepsilon\partial_Z q_1 + \varepsilon^2\partial_Z q = \varepsilon\partial_X(\tau_{ZX}) + \varepsilon\partial_Z(\tau_{ZZ}), \tag{10}$$

where the gravitational term has been cancelled with the hydrostatic contribution of the pressure. Note that the previous equation (10) involves the first and second order terms of the non-hydrostatic pressure q, q_1 balanced by the a term related to the vertical acceleration (left hand side) and a term coming from the stress tensor (right hand side). Now, by comparing the terms with same order of magnitude in equation (10), we obtain that

$$\partial_Z q_1 = \partial_X(\tau_{ZX}) + \partial_Z(\tau_{ZZ}), \tag{11}$$

and

$$-\partial_Z q = \rho\big(\partial_t w + u\,\partial_X w + w\,\partial_Z w\big). \tag{12}$$

In this work, the aim is to obtain the simplest depth-averaged non-hydrostatic model, improving the results of hydrostatic models. First, from the numerical point of view, it is difficult to deal with the viscous terms in (11). Second, the problem of considering the vertical acceleration has been widely studied for shallow water flows, both from the modeling and the numerical point of view. Thus, we are

going to neglect the first order terms of the pressure and keep the second order contribution, i.e., we keep (12) and do not consider (11). In the numerical tests, we will show that this choice significantly improves the results compared to the hydrostatic assumption.

Next, we derive the final model by integrating (8a),(8b) and (12) along the vertical direction. To this aim, for any variable f we define its average on the normal direction by

$$\overline{f} = \frac{1}{h}\int_b^{b+h} f dZ.$$

We shall use that $\overline{f \cdot g} = \overline{f} \cdot \overline{g}$, which is true up to first order. Then, by integrating on the normal direction equations (8a) and (12) between b and $b+h$, and taking into account the Leibniz's rule, we get

$$\partial_X\left(h\overline{u}\right) + \left(u_{|_b}\partial_X b - w_{|_b}\right) - \left(u_{|_{b+h}}\partial_X\left(b+h\right) - w_{|_{b+h}}\right) = 0,$$

$$\partial_t\left(h\overline{w}\right) + \partial_X\left(h\overline{u}\,\overline{w}\right) + w_{|_b}\left(u_{|_b}\partial_X b - w_{|_b}\right) - w_{|_{b+h}}\left(\partial_t\left(b+h\right) + u_{|_{b+h}}\partial_X\left(b+h\right) - w_{|_{b+h}}\right) = \frac{1}{\rho}q_{|_b}.$$

Using now the kinematic and non-penetration conditions we get

$$\begin{aligned} \partial_t h + \partial_X\left(h\overline{u}\right) &= 0, \\ \partial_t\left(h\overline{w}\right) + \partial_X\left(h\overline{u}\,\overline{w}\right) &= \frac{1}{\rho}q_{|_b}. \end{aligned} \tag{13}$$

A closure relation is needed for the non-hydrostatic pressure. For the sake of simplicity, we shall assume that $p_T(X,\cdot,t)$ has a linear profile. This hypothesis implies that $q_{|_b} = 2\overline{q}$. Then, as a consequence, the system has only one extra unknown, $\overline{q}$. Nevertheless, other possible choices may be made on the profile of the non-hydrostatic pressure. This would mean then that the system will have extra unknowns and equations (see e.g. [24, 19]).

We focus now on the horizontal momentum equation (8b) up to first order. Noticing that

$$\int_b^{b+h}\partial_X p_T\, dz = \frac{\rho}{Fr^2}h\partial_X\left(b+h\right) + \varepsilon^2\left(\partial_X\left(h\overline{q}\right) + q_{|_b}\partial_X b\right),$$

and using $q_b = 2\overline{q}$, the depth-averaged momentum conservation equation is

$$\begin{aligned} \rho\left(\partial_t\left(h\overline{u}\right) + \partial_X\left(h\overline{u}^2\right) + \frac{1}{Fr^2}h\partial_X\left(h + b + \frac{x\tan\theta}{\varepsilon}\right)\right) = \\ -\varepsilon^2\left(\partial_X\left(h\overline{q}\right) + 2\overline{q}\partial_X b\right) - \frac{1}{\varepsilon}\mu(I_{|_b})p_{T|_b}\frac{\overline{u}}{|\overline{u}|} \end{aligned} \tag{14}$$

where the friction condition (9) has been used.

Considering equations (13) and (14), we have a system with 3 equations and 4 unknowns (h,u,w,q). Then, in order to close the system, we integrate the continuity equation (8a) between the bottom (b)

and the midpoint of the layer $(b+h/2)$, obtaining (by using the Leibniz's rule and the non-penetration condition)

$$\partial_X \left(\int_b^{b+h/2} u dz \right) - u_{|_{b+h/2}} \partial_X \left(b + h/2 \right) + w_{|_{b+h/2}} = 0.$$

Notice that

$$\overline{u} = u_{|_{b+h/2}} + \mathcal{O}(\varepsilon^2), \quad \int_b^{b+h/2} u dz = \frac{h\overline{u}}{2} + \mathcal{O}(\varepsilon) \quad \text{and} \quad \overline{w} = w_{|_{b+h/2}} + \mathcal{O}(\varepsilon^2),$$

thanks to the midpoint and the rectangular quadrature rule to approximate those integrals. Then, we obtain that

$$\overline{w} = \overline{u}\partial_X b - \frac{h}{2}\partial_X \overline{u}. \tag{15}$$

The resulting system is equivalent to an optimization problem consisting of the minimization of the energy subject to the constraint (15), at least for a semi-discrete version of the momentum equation (14) (see for example [21]). In this sense $q_{|_b} = 2\bar{q}$ may be seen as the Lagrange multiplier associated to the constraint (15).

In the final model, equation (15) is multiplied by h in order to write the system in terms of the conservative variables (see (16d)).

2.3 Final model

Collecting the equations that we have obtained in previous subsections and going back to dimensional variables, we get the system

$$\begin{cases} \partial_t h + \partial_X \left(h\overline{u} \right) = 0, & \text{(16a)} \\ \rho \left(\partial_t \left(h\overline{u} \right) + \partial_X \left(h\overline{u}^2 \right) + g\cos\theta h \partial_X \left(h + b + \widetilde{b} \right) \right) \\ \qquad = -\left(\partial_X \left(h\bar{q} \right) + 2\bar{q}\partial_X b \right) - \tau_{XZ|_b}, & \text{(16b)} \\ \rho \left(\partial_t \left(h\overline{w} \right) + \partial_X \left(h\overline{u}\overline{w} \right) \right) = 2\bar{q}, & \text{(16c)} \\ h\overline{w} = h\overline{u}\partial_X b - \dfrac{h}{2}\partial_X h\overline{u} + \dfrac{h\overline{u}}{2}\partial_x h, & \text{(16d)} \end{cases}$$

where

$$\tau_{XZ|_b} = \begin{cases} \mu(I_{|_b}) p_{T|_b} \dfrac{\overline{u}}{|\overline{u}|} & \text{if } |u| \neq 0, \\ \left| \tau_{XZ|_b} \right| \leq \mu_s p_T & \text{if } |u| = 0, \end{cases} \tag{16e}$$

and $\mu(I)$ is given by (6), and

$$I_{|_b} = \frac{d_s \left| (\partial_z u)_{|_b} \right|}{\sqrt{p_{T_{|_b}}/\rho_s}}, \quad \text{with} \quad p_{T|_b}/\rho_s = \frac{\rho}{\rho_s} \left(g\cos\theta h + 2\frac{\bar{q}}{\rho} \right) = \varphi_s \left(g\cos\theta h + 2\frac{\bar{q}}{\rho} \right). \tag{16f}$$

Note that the friction term is computed taking into account the total pressure, hydrostatic and non-hydrostatic. In order to simplify system (16), in what follows we shall redefine the non-hydrostatic variable as $\overline{q} = \overline{q}/\rho$. In the next section, we detail the numerical scheme proposed to approximate system (16).

Remark 1. *A hydrostatic version of model (16) is obtained from (16a), (16b) and (16f), by setting $\overline{q} = 0$. The resulting hydrostatic model corresponds to the one proposed in [47], which is the Savage-Hutter model [51], where the friction coefficient is improved by using the $\mu(I)$ rheology. This model also matches to the one proposed in [26] when the the viscous term $\partial_X \tau_{XX}$ is removed.*

Remark 2. *Concerning steady states for system (16), we shall focus on stationary solution when the granular flow is at rest. Writing the momentum equation (16b) with $\bar{u} = \bar{w} = \bar{q} = 0$, and taking absolute values we get*

$$\rho g \cos\theta h \left|\partial_X \left(h + b + \widetilde{b}\right)\right| = \left|\tau_{XZ|_{b,u=0}}\right| \leq \left|\mu(I_{|_{b,u=0}}) p_{T|_{b,u=0}}\right| = \rho g \cos\theta h \mu_s.$$

Therefore, these stationary solutions take the form

$$\bar{u} = \bar{w} = \bar{q} = 0, \quad \textit{and} \quad \left|\partial_X \left(h + b + \widetilde{b}\right)\right| \leq \mu_s. \tag{17}$$

Note that previous equation corresponds to solutions at rest for classical Savage-Hutter model. When designing a numerical scheme for model (16) we will be interested in preserving these steady states, that is, a well-balanced scheme for (17).

3 Numerical approximation

One of the aims of this paper is to propose a simple and efficient numerical scheme to approximate the previously introduced non-hydrostatic shallow $\mu(I)$-model (16). We propose a numerical approximation consisting in a three-steps method, where the main novelty is how to deal with the Coulomb friction term together with the non-hydrostatic pressure. The first step involves the hyperbolic part of the system and an explicit discretization of the non-hydrostatic term. In this first step a path-conservative finite volume scheme is considered, together with a hydrostatic reconstruction in order to ensure the well-balance property. Secondly, the Coulomb friction is added taking into account also the non-hydrostatic contributions. Finally, a non-hydrostatic pressure deviation in time is computed and the velocity field is corrected accordingly.

Regarding the computational cost of this non-hydrostatic model, it was shown that using the strategy in Escalante *et al.* [18], the computational effort associated to a non-hydrostatic model for shallow water flows is approximately 2.4 times greater than the one for the hydrostatic version of the model. Similar results are expected here for the proposed model (16). In what follows we shall describe each step in detail.

Let us denote by $\mathbf{U} = (h, hu, hw)^{'}$. We consider a usual Finite Volume discretization, where the horizontal domain is divided in control volumes $V_i = \left[x_{i-1/2}, x_{i+1/2}\right]$, for $i \in \mathcal{I}$. For the sake of simplicity we assume a fixed volume mesh size Δx. We denote the center of each volume cell by $x_i = \left(x_{i-1/2} + x_{i+1/2}\right)/2$. For any time t, we consider the cell averages

$$\mathbf{U}_i(t) = \frac{1}{\Delta x} \int_{x_{i-1/2}}^{x_{i+1/2}} \mathbf{U}(x,t) dx.$$

Regarding non-hydrostatic terms, a staggered grid is considered formed by the points $x_{i-1/2}, x_{i+1/2}$ of the interfaces for each cell V_i. Let us denote the approximation of the point values of the function q representing the non-hydrostatic pressure on point $x_{i+1/2}$ at time t by

$$q_{i+1/2}(t) = q(x_{i+1/2}, t).$$

Remark that this corresponds to a second order approximation of the cell average of the pressure on the staggered grid $[x_i, x_{i+1}]$. In what follows and for the sake of simplicity, we omit the dependence on the time t.

In order to define a numerical scheme for (18), we have to consider the following three key points:

- The resulting scheme should be well-balanced for (17). This is achieved by means of a hydrostatic reconstruction procedure, taking into account friction terms (see [23]).
- The friction contribution should be taken into account before solving the non-hydrostatic pressure. Otherwise, the incompressibility condition is not ensured.
- Both, hydrostatic and non-hydrostatic pressures, should be considered when dealing with the friction term.

We propose here a numerical scheme based on three steps which are described in what follows.

Step 1: Hyperbolic problem

The first step focuses on solving the hyperbolic system obtained when friction and non-hydrostatic effects are removed from system (16). Therefore, we obtain the following system (bars are dropped for simplicity):

$$\begin{cases} \partial_t h + \partial_X (hu) = 0, & \text{(18a)} \\ \partial_t (hu) + \partial_X \left(hu^2\right) + g\cos\theta h \partial_X \left(h + b + \widetilde{b}\right) = 0, & \text{(18b)} \\ \partial_t (hw) + \partial_X (huw) = 0. & \text{(18c)} \end{cases}$$

We see that equations (18a) and (18b) correspond to a shallow water system, combined with a transport equation for a passive scalar (18c). In order to solve system (18), we follow a similar approach as in [25]. In particular, we follow the path-conservative framework [41] to define a HLL-type method for the shallow water system in a similar way as it is done in [23]. After that, the third equation is considered as a transport equation of a passive scalar. For the sake of completeness, let us describe this in detail.

System (18a)-(18b) may be written in compact form as

$$\partial_t \mathbf{W} + \partial_X \mathbf{F_c}(\mathbf{W}) + \mathbf{S}(\mathbf{W}) \partial_X \left(\widetilde{b} + b + h\right) = \mathbf{0} \quad \text{(19a)}$$

$$\partial_t (hw) + \partial_X (huw) = 0, \quad \text{(19b)}$$

where $\mathbf{W} = (h, hu)^{'} \in \mathbb{R}^2$, $\mathbf{F_c}(\mathbf{W}) = (hu, hu^2)^{'}$ is the convective part of the flux and $\mathbf{S}(\mathbf{W}) = (0, g\cos\theta h)^{'}$ defines the source term which accounts for the hydrostatic pressure.

Then, the finite volume method is described as

$$\mathbf{W}_i^{n+1/3} = \mathbf{W}_i^n + \frac{\Delta t}{\Delta x}\left(\boldsymbol{\mathcal{F}}_{i-1/2}^n - \boldsymbol{\mathcal{F}}_{i+1/2}^n + \frac{1}{2}\left(\boldsymbol{\mathcal{S}}_{i+1/2}^n + \boldsymbol{\mathcal{S}}_{i-1/2}^n\right)\right), \tag{20}$$

with

$$\boldsymbol{\mathcal{S}}_{i+1/2}^n = \frac{1}{2}(\mathbf{S}(\mathbf{W}_{i+1}^n) + \mathbf{S}(\mathbf{W}_i^n))\Delta\eta_{i+1/2}^n, \tag{21}$$

where $\Delta\eta_{i+1/2}^n = \left(\widetilde{b}+b+h\right)_{i+1}^n - \left(\widetilde{b}+b+h\right)_i^n$. Finally, the numerical flux corresponding to the convective terms $\boldsymbol{\mathcal{F}}_{i+1/2}^n$, is

$$\boldsymbol{\mathcal{F}}_{i+1/2}^n = \frac{1}{2}\left(\mathbf{F_c}(\mathbf{W}_{i+1}^n) + \mathbf{F_c}(\mathbf{W}_i^n)\right) - \frac{1}{2}\boldsymbol{\mathcal{D}}_{i+1/2}^n,$$

where $\boldsymbol{\mathcal{D}}_{i+1/2}^n$ is the numerical diffusion of the scheme.

Here we use the framework of Polynomial Viscosity Methods (PVM) introduced in [12] in order to define the numerical diffusion term. In particular, we use a generalization of the HLL scheme for non-conservative hyperbolic systems where

$$\boldsymbol{\mathcal{D}}_{i+1/2} = \alpha_0\left(\widehat{\mathbf{W}}_{i+1/2}^+ - \widehat{\mathbf{W}}_{i+1/2}^-\right) + \alpha_1\left(\mathbf{F_c}(\mathbf{W}_{i+1}^n) - \mathbf{F_c}(\mathbf{W}_i^n) + \widehat{\boldsymbol{\mathcal{S}}}_{i+1/2}^n\right), \tag{22}$$

with

$$\widehat{\boldsymbol{\mathcal{S}}}_{i+1/2}^n = \frac{1}{2}(\mathbf{S}(\mathbf{W}_{i+1}^n) + \mathbf{S}(\mathbf{W}_i^n))\left(\widehat{h}_{i+1/2}^{+,n} - \widehat{h}_{i+1/2}^{-,n}\right),$$

where the definition of $\widehat{\mathbf{W}}_{i+1/2}^{\pm}$, which will be given in equation (24), is a key point in order to preserve steady state solutions (17), and

$$\alpha_0 = \frac{S_R|S_L| - S_L|S_R|}{S_R - S_L}, \quad \alpha_1 = \frac{|S_R| - |S_L|}{S_R - S_L},$$

being S_L and S_R approximations of the minimum and maximum wave speed. In practice,

$$S_L = \min\left(u_i - \sqrt{g\cos\theta h_i},\, u_{i+1/2} - \sqrt{g\cos\theta h_{i+1/2}}\right),$$

$$S_R = \max\left(u_{i+1} + \sqrt{g\cos\theta h_{i+1}},\, u_{i+1/2} + \sqrt{g\cos\theta h_{i+1/2}}\right),$$

where $h_{i+1/2}, u_{i+1/2}$ are the usual Roe's averaged states for Shallow Water system.

One of the difficulties of this method is to ensure the well-balance property for (17). In particular, we find in (17) two types of steady states. On the one hand we have the ones corresponding of lake at rest in Shallow Water, where $\partial_X\left(h+b+\widetilde{b}\right) = 0$. In this case the well-known hydrostatic reconstruction [2] provides a tool based on reconstructed states that would allow us to cancel the numerical diffusion in such situations, and resulting in a well-balanced scheme. On the other hand, we have the family of steady states where $\partial_X\left(h+b+\widetilde{b}\right) \neq 0$, which correspond to granular flows at rest for which the

friction force is greater than pressure forces. In that case, the classical hydrostatic reconstruction is not enough to preserve those steady states. In [4], a modification of the original hydrostatic reconstruction is presented with the goal of canceling the numerical diffusion associated to the approximated Riemann solver in that case, in order to ensure $\partial_t h = 0$ when the granular flow is at rest ($u = 0$). Here we use similar ideas. We define the following reconstructed states: for every interface $x_{i+1/2}$ we define

$$\begin{aligned} h^-_{i+1/2} &= \max(0, h_i - (\Delta Z_{i+1/2})_+); \\ h^+_{i+1/2} &= \max(0, h_{i+1} - (-\Delta Z_{i+1/2})_+), \end{aligned} \quad \text{with} \quad (\Delta Z_{i+1/2})_+ = \max(0, z_{b,i+1} - z_{b,i}). \tag{23}$$

and

$$\widehat{\mathbf{W}}^-_{i+1/2} = \left(\widehat{h}^-_{i+1/2}, \widehat{h}^-_{i+1/2} u_i\right), \qquad \widehat{\mathbf{W}}^+_{i+1/2} = \left(\widehat{h}^+_{i+1/2}, \widehat{h}^+_{i+1/2} u_{i+1}\right), \tag{24}$$

in (22), where $\widehat{h}^\pm_{i+1/2}$ are defined as in (23), taking in this case

$$(\Delta Z_{i+1/2})_+ = \max(0, z_{b,i+1} - z_{b,i} + \Delta \mathcal{C}_{i+1/2}), \tag{25}$$

with $\Delta \mathcal{C}_{i+1/2} = -f_{i+1/2}\Delta x / (g \cos\theta)$ defined in terms of the Coulomb friction (see [4]). We set

$$f_{i+1/2} = - \underset{g\cos\theta\mu(I_{|_b})}{proj} \left(\frac{-g\cos\theta(h_{i+1} + z_{b,i+1} - h_i - z_{b,i})}{\Delta x} + \frac{u_{i+1/2}}{\Delta t} \right), \tag{26}$$

where

$$\underset{g\cos\theta\mu(I_{|_b})}{proj}(X) = \begin{cases} X & \text{if} \quad |X| \le g\cos\theta\mu(I_{|_b}); \\ g\cos\theta\mu(I_{|_b}) \dfrac{X}{|X|} & \text{if} \quad |X| > g\cos\theta\mu(I_{|_b}), \end{cases} \tag{27}$$

although other definitions of $f_{i+1/2}$ can be used (see [4]).

Once the numerical flux for the two first components is computed, we define the third one by

$$(hw)^{n+1/3}_i = (hw)^n_i + \frac{\Delta t}{\Delta x}\left(\boldsymbol{\mathcal{F}}^{hw,n}_{i-1/2} - \boldsymbol{\mathcal{F}}^{hw,n}_{i+1/2}\right), \tag{28}$$

where the flux for this component is

$$\boldsymbol{\mathcal{F}}^{hw,n}_{i+1/2} = \left[\boldsymbol{\mathcal{F}}^n_{i+1/2}\right]_h w^{up,n}_{i+1/2}, \quad \text{with} \quad w^{up}_{i+1/2} = \begin{cases} w_i & \text{if} \quad \left[\boldsymbol{\mathcal{F}}_{i+1/2}\right]_h > 0 \\ w_{i+1} & \text{if} \quad \left[\boldsymbol{\mathcal{F}}_{i+1/2}\right]_h < 0, \end{cases}$$

where $\left[\boldsymbol{\mathcal{F}}^n_{i+1/2}\right]_h$, that approximates $(hu)_{i+1/2}$, denotes the first component of the numerical flux $\boldsymbol{\mathcal{F}}^n_{i+1/2}$.

Remark 3. *It is a known fact, in the context of Shallow Water, that care has to be taken in the cases of emerging bottom. For instance, in the lake at rest configuration with $h_{i+1} = 0$ and $h_i + b_i < b_{i+1}$, the term $\Delta\eta_{i+1/2}$ in (21) produces an artificial pressure term at the right cell, which makes well-balancing to fail. A posibility to overcome this difficulty is to rewrite the bottom on the right cell to equilibrate pressure terms (see [11]). In practice, we replace $\Delta\eta^n_{i+1/2}$ in (21) by $h^{+,n}_{i+1/2} - h^{-,n}_{i+1/2}$, where these reconstructed states are defined by (23).*

Step 2: Coulomb friction term

In order to introduce the Coulomb friction term, we consider a semi-implicit scheme with an appropriate stopping criteria. From the physical point of view, the friction is a force that opposes the movement of the granular mass. When this friction is greater than the rest of the forces, then the flow must stop. The numerical treatment is based on this idea, which will be summarized in what follows. We refer the reader to [39, 20] for further details.

We set $h_i^{n+2/3} = h_i^{n+1/3}$, and define $\widetilde{h}_i^n = \left(h_{i-1/2}^n + h_{i+1/2}^n\right)/2$,

$$\sigma_{c,i}^n = \mu(I_{|_b}^n)\left(g\cos\theta\widetilde{h}_i^n + 2q_i^n\right), \quad \text{with} \quad q_i^n = \left(q_{i-1/2}^n + q_{i+1/2}^n\right)/2,$$

$$(hu)_i^{\star,n+1/3} = (hu)_i^{n+1/3} - \Delta t\left(h_i^n\left(\partial_X q^n\right)_i + q_i^n\partial_X\left(2b+h^n\right)_i\right)$$

with

$$\left(\partial_X q\right)_i = \frac{q_{i+1}-q_i}{\Delta x}, \quad \left(\partial_X\left(2b+h\right)\right)_i = \frac{(2b+h)_{i+1} - (2b+h)_{i-1}}{2\Delta x}.$$

Then, the new values at this second step for the horizontal and vertical discharges are

$$\begin{cases} (hu)_i^{n+2/3} = (hu)_i^{\star,n+1/3} - \Delta t\,\sigma_{c,i}^n\, SGN\left((hu)_i^{\star,n+1/3}\right), \\ \qquad\qquad\qquad\qquad\qquad\qquad\qquad\qquad \text{if} \quad \Delta t\,\sigma_{c,i}^n < \left|(hu)_i^{\star,n+1/3}\right|; \\ (hw)_i^{n+2/3} = (hw)_i^{n+1/3} + 2\Delta t q_i^n, \end{cases}$$

otherwise

$$(hu)_i^{n+2/3} = 0, \quad \text{and} \quad (hw)_i^{n+2/3} = 0,$$

where SGN is the sign function.

Step 3: Non-hydrostatic pressure correction

In the last step the non-hydrostatic effects are added using the momentum equations (16b),(16c) together with the incompressibility condition (16d).

Taking into account system (16), we set $h^{n+1} = h^{n+2/3} = h^{n+1/3}$ and define

$$\tilde{q} = q^{n+1} - q^n.$$

Then we consider a projection method and we get

$$(hu)^{n+1} = (hu)^{n+2/3} - \Delta t\left(\partial_X\left(h^{n+1}\tilde{q}\right) + 2\tilde{q}\partial_X b\right), \tag{29}$$

$$(hw)^{n+1} = (hw)^{n+2/3} + 2\,\Delta t\,\tilde{q}. \tag{30}$$

and the depth-averaged incompressibility equation

$$(hw)^{n+1} = (hu)^{n+1}\,\partial_X b - \frac{h^{n+1}}{2}\partial_X\,(hu)^{n+1} + \frac{(hu)^{n+1}}{2}\partial_X h^{n+1}. \tag{31}$$

Now, putting equations (29),(30) into (31) and after some straightforward algebra, the following elliptic equation is deduced for $\tilde{q}$,

$$\begin{aligned}\left(h^{n+1}\right)^2 \partial_{XX}\tilde{q} \;+\; & h^{n+1}\partial_X h^{n+1}\partial_X\tilde{q} + \Big(h^{n+1}\partial_{XX}\left(2b+h^{n+1}\right) - \left(\partial_X\left(2b+h^{n+1}\right)\right)^2 - 4\Big)\tilde{q} \\ = \;& \frac{1}{\Delta t}\Big(2\,(hw)^{n+2/3} - (hu)^{n+2/3}\,\partial_X\left(2b+h^{n+1}\right) + h^{n+1}\partial_X\,(hu)^{n+2/3}\Big). \qquad (32)\end{aligned}$$

Finally, this equation is discretized in space at the interfaces $x_{i+1/2}$. Let us recall that the variables (h), (hu), and (hw) are computed as averages in the control volumes, while (q) is computed as point values at the interfaces. Therefore, we set

$$h_{i+1/2} = \frac{h_i + h_{i+1}}{2}, \qquad (hu)_{i+1/2} = \frac{(hu)_i + (hu)_{i+1}}{2}, \qquad (hw)_{i+1/2} = \frac{(hw)_i + (hw)_{i+1}}{2},$$

and we approximate of the derivative of the non-hydrostatic pressure deviation by

$$(\partial_{XX}\tilde{q})_{i+1/2} = \frac{\tilde{q}_{i+3/2} - 2\tilde{q}_{i+1/2} + \tilde{q}_{i-1/2}}{\Delta x^2} \qquad (\partial_X\tilde{q})_{i+1/2} = \frac{\tilde{q}_{i+1/2} - \tilde{q}_{i-1/2}}{2\Delta x}.$$

Moreover, we set

$$(\partial_X h)_{i+1/2} = \frac{h_{i+1} - h_i}{\Delta x}, \qquad (\partial_X b)_{i+1/2} = \frac{b_{i+1} - b_i}{\Delta x},$$

and

$$\left(\partial_{XX}\left(2b+h\right)\right)_{i+1/2} = minmod\left(\Delta^+_{2b+h}, \Delta^c_{2b+h}, \Delta^-_{2b+h}\right),$$

where

$$\Delta^+_{2b+h} = \frac{\partial_X\left(2b+h\right)_{i+3/2} - \partial_X\left(2b+h\right)_{i+1/2}}{\Delta x}, \quad \Delta^-_{2b+h} = \frac{\partial_X\left(2b+h\right)_{i+1/2} - \partial_X\left(2b+h\right)_{i-1/2}}{\Delta x},$$

and $\Delta^c_{2b+h} = \left(\Delta^+_{2b+h} + \Delta^-_{2b+h}\right)/2$.

Then, a tridiagonal linear system is obtained for the unknown values $\{\tilde{q}_{i+1/2}\}_i$. Once this linear system is solved, the values of $\left\{\left((hu)_i^{n+1}, (hw)_i^{n+1}, q_{i+1/2}^{n+1}\right)\right\}_{i\in\mathcal{I}}$ are updated using (29) and (30), leading to

$$\begin{aligned}(hu)_i^{n+1} &= (hu)_i^{n+2/3} \;-\; \Delta t\left(h_i^{n+1}\left(\partial_X\tilde{q}\right)_i + \tilde{q}_i\partial_X\left(2b+h^{n+1}\right)_i\right), \\ (hw)_i^{n+1} &= (hw)_i^{n+2/3} \;+\; 2\,\Delta t\tilde{q}_i, \\ q_{i+1/2}^{n+1} &= \tilde{q}_{i+1/2} + q_{i+1/2}^n,\end{aligned}$$

with

$$\tilde{q}_i = \frac{\tilde{q}_{i-1/2} + \tilde{q}_{i+1/2}}{2}, \qquad (\partial_X\tilde{q})_i = \frac{\tilde{q}_{i+1} - \tilde{q}_i}{\Delta x}, \quad \left(\partial_X\left(2b+h\right)\right)_i = \frac{\left(2b+h\right)_{i+1} - \left(2b+h\right)_{i-1}}{2\Delta x}.$$

Theorem 1. *The scheme defined by steps 1, 2 and 3 is exactly well-balanced for steady solutions given by*

$$u = w = q = 0, \qquad \left|\partial_X \left(\widetilde{b} + b + h\right)\right| = \tan\theta, \qquad \text{with} \qquad 0 \leq \theta \leq \arctan \mu_s.$$

In particular, in the limit case $\left|\partial_X \left(\widetilde{b} + b + h\right)\right| = \mu_s$.

Proof. Remark that it is sufficient to prove that the steps 1 and 2 do not modify the initial state, since from (32) the non-hydrostatic pressure is zero when the discharges are zero.

Let us focus first on the first step. From the definition of (24) and taking into account that $u = 0$, it follows that $\widehat{\mathbf{W}}^{+}_{i+1/2} = \widehat{\mathbf{W}}^{-}_{i+1/2}$. Therefore, the numerical diffusion (22) vanishes. As a consequence, $h_i^{n+1/3} = h_i^n$ from (20). Moreover, since steps 2 and 3 do not modify the first component, we get $h_i^{n+1} = h_i^n$. Note also that $(hw)_i^{n+1/3} = (hw)_i^n = 0$ thanks to (28).

Let us focus now on the second component,

$$(hu)_i^{n+1/3} = (hu)_i^n - \frac{1}{2} g \cos\theta \frac{\Delta t}{\Delta x} \left(\left(h_i^n + h_{i-1}^n\right) \Delta\eta_{i-1/2}^n + \left(h_{i+1}^n + h_i^n\right) \Delta\eta_{i+1/2}^n \right).$$

Noticing that the profile of the free surface is linear, i.e, $\Delta\eta_{i+1/2}^n/\Delta x = \tan\theta$ and $(hu)_i^n = 0$, this leads to

$$(hu)_i^{n+1/3} = -g\cos\theta\Delta t \left(h_i^n + \frac{1}{2}\left(h_{i-1}^n + h_{i+1}^n\right)\right) \tan\theta = -g\cos\theta\Delta t \widetilde{h}_i^n \tan\theta.$$

In the second step, since the velocity and the non-hydrostatic pressure are both zero, we have that

$$\sigma_{c,i}^n = g\cos\theta\mu_s \widetilde{h}_i^n, \qquad \text{and} \qquad (hu)_i^{\star,n+1/3} = (hu)_i^{n+1/3}.$$

Then, taking into account that $\tan\theta \leq \mu_s$, it yields

$$\left|(hu)_i^{n+1/3}\right| = g\cos\theta\Delta t\widetilde{h}_i^n \tan\theta \leq g\cos\theta\Delta t\widetilde{h}_i^n \mu_s = \Delta t \sigma_{c,i}^n, \tag{33}$$

obtaining then $(hu)_i^{n+2/3} = (hw)_i^{n+2/3} = 0$, and therefore $(h, hu, hw)_i^{n+1} = (h, 0, 0)_i^n$, which concludes the proof.

□ □

Corollary 1. *The scheme defined by steps 1, 2 and 3 preserves the discrete steady states at rest, i.e., those verifying*

$$u_i = w_i = q_i = 0, \qquad \left| \frac{\left(\widetilde{b} + b + h\right)_{i+1} - \left(\widetilde{b} + b + h\right)_i}{\Delta x} \right| \leq \mu_s \qquad \text{for all } i \in \mathcal{I}.$$

Proof. It follows from the proof of Theorem 1. □ □

Table 1: Rheological parameters considered in all the numerical tests.

d_s (mm)	μ_s	μ_2	I_0	φ_s
0.7	$\tan(25.5°) \simeq 0.48$	$\tan(36°) \simeq 0.73$	0.279	0.62

Remark 4. *When considering the continuous steady states (17) in the general case, we have that*

$$\frac{\left(\widetilde{b}+b+h\right)_{i+1}-\left(\widetilde{b}+b+h\right)_{i}}{\Delta x}=\left[\partial_X\left(\widetilde{b}+b+h\right)\right]_{i+1/2}+\mathcal{O}\left(\Delta x^2\right).$$

If $\left|\partial_X\left(\widetilde{b}+b+h\right)\right|<\mu_s$*, then the hypothesis of previous corollary is true for a sufficiently small* Δx*. Otherwise, when the equality holds, one should take care with the proof of Theorem 1. In particular,* $\widehat{\mathbf{W}}^{+}_{i+1/2}=\widehat{\mathbf{W}}^{-}_{i+1/2}$ *and inequality (33) are both true up to a second order term in* Δx*.*

4 Numerical tests

In this section, we present some numerical tests in order to validate the non-hydrostatic model and the numerical approach introduced in this paper. Comparisons with a hydrostatic version of the proposed model (see Remark 1) will be shown.

First, we study the influence of the choice of the coordinate system (local or Cartesian) when using the hydrostatic and the non-hydrostatic model. In a second series of tests, we compare with experimental data of granular collapse over inclined planes described in [37]. Comparisons are carried out using both the hydrostatic and non-hydrostatic models in local coordinates.

Notice that, in this section, whenever we speak about hydrostatic/non-hydrostatic model in local or Cartesian coordinates, we refer to the direction along which the shallowness approximation is applied and the depth-average procedure is performed starting from the 2D Navier-Stokes system. This direction is normal to the reference plane $\widetilde{b}$ for local coordinates and in the vertical z-direction for the Cartesian coordinates.

All the simulations are carried out with a constant mesh size, Δx, and an adaptive time step, Δt, computed with

$$CFL=\max_{i\in\mathcal{I}}\left(|u_i|+\sqrt{g\cos\theta h_i}\right)\frac{\Delta t}{\Delta x}=0.5.$$

Regarding boundary conditions, a ghost cell technique is used to impose wall boundary conditions upstream for the hyperbolic problem, and homogeneous Neumann condition for the elliptic problem. In all the tests shown here there is a vacuum zone downstream. In addition, thanks to the fact that the incompressibility equation (15) is multiplied by h to obtain (16d), the solution of the elliptic problem naturally degenerates to $\bar{q}=0$ in vacuum zones. This is done for all the presented tests. The rheological parameters of the granular material are given in Table 1.

4.1 Well-balanced test for arbitrary bottom

Let us start by checking that the proposed scheme is well-balanced for not flat solutions given by (17). To this aim, we consider here a computational domain $[-3,1]$ with 300 points, where the bottom is

given by $\widetilde{b} = 0$ and

$$b_1(x) = \frac{2}{x+4} - 0.5 + 0.25\,\mathrm{RAND}(x), \quad b_2 = 0.6 - 6.5(x-1.5)^2, \qquad b(x) = \begin{cases} b_1 + b_2 & \text{if } b_1 < b_2, \\ b_1 & \text{otherwise,} \end{cases}$$

where $\mathrm{RAND}(x) \in [0,1]$ is a random value generated at run time. The free surface is given by (see Figure 2)

$$h(x) + b(x) = \max\left(-0.45 - (x-2)\mu_s, b(x)\right),$$

where in this case $\mu_s = \tan(20^\circ)$, and the discharges hu, hw are set to zero.

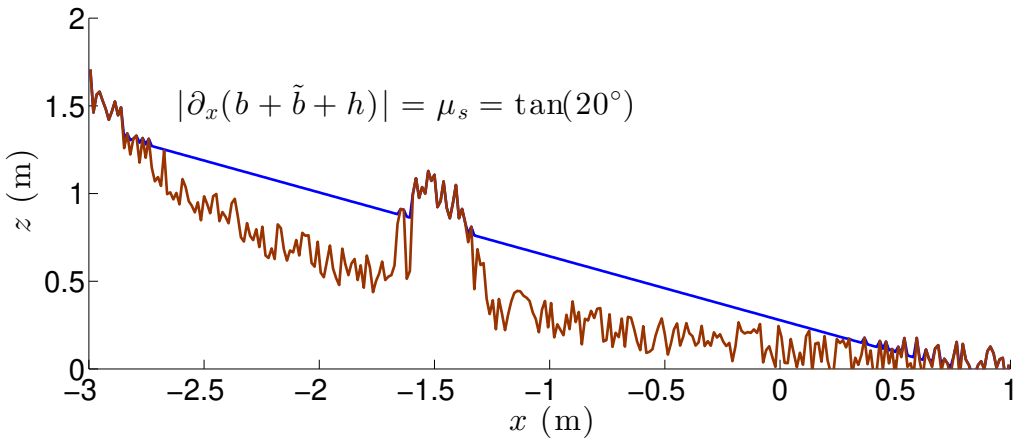

Figure 2: Bottom and free surface for the well-balanced test.

In this case, the L^1 and L^2 errors between the initial and final heights are 6.4×10^{-15} and 7.5×10^{-16} respectively. For hu and hw the errors are zero thanks to the treatment described in step 2 of the numerical approximation. Moreover, we have checked that the previous initial condition is not stationary if the angle of repose is lower that 20°. Therefore, we can conclude that the scheme is well-balanced for steady states given by (17).

4.2 Convergence test

In this test we perform a convergence test showing that the proposed scheme is indeed first order accurate for time dependent solutions.

It is well-known that non-hydrostatic simulation for shallow water equations produces an overshooting in the presence of shock when using very fine meshes. This non-physical effect makes it difficult to study convergence of the scheme when this situation arises. In order to avoid this problem, we consider here a smooth initial condition for the height with no wet-dry fronts, starting from the rest, over an slope given by $b(X) = 0$,

$$\widetilde{b}(x) = (2.7 - x)\tan 20^\circ, \qquad \text{and} \quad h(X) = 0.02 + 0.4\,e^{-5(X-0.25)^2},$$

in the computational domain $[-0.5, 2.7]$. The material properties are in Table 1.

We compute the L^1 errors and numerical orders for the conservative variables (h, hu, hw) in an intermediate time, before overshooting occurs. To this aim, the reference solution is computed with

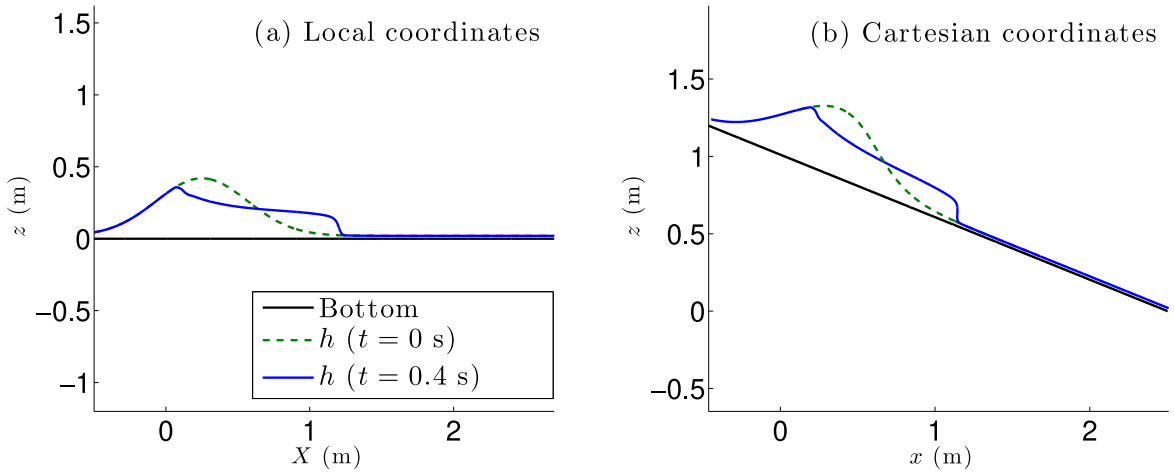

Figure 3: Height profiles at initial time (dashed green lines) and at $t = 0.4$ s (solid blue lines) in (a) local and (b) Cartesian coordinates.

N. cells	Error h	Order h	Error hu	Order hu	Error hw	Order hw
25	2.20×10^{-2}		2.94×10^{-2}		1.33×10^{-2}	
50	1.62×10^{-2}	0.45	2.00×10^{-2}	0.55	1.07×10^{-2}	0.32
100	1.11×10^{-2}	0.54	1.34×10^{-2}	0.59	7.90×10^{-3}	0.44
200	6.66×10^{-3}	0.74	7.66×10^{-3}	0.80	5.74×10^{-3}	0.46
400	3.81×10^{-3}	0.81	4.16×10^{-3}	0.88	3.61×10^{-3}	0.67
800	1.88×10^{-3}	1.02	1.94×10^{-3}	1.10	1.84×10^{-3}	0.98

Table 2: L^1 *Errors and related orders for the height* (h) *and the discharges* (hu, hw) *for the solution at time* $t = 0.4$ *s.*

3200 nodes. Figure 3 shows the initial condition and the height at time $t = 0.4$ s, where the errors are measured. The results can be seen in table 2, where we obtain that the proposed scheme is first order accurate for all the variables.

4.3 Influence of the coordinate system

In this test, we first propose to analyze how much the use of local coordinates is important. To do so, let us compare the results obtained when one uses local or Cartesian coordinates. The simulations will be performed using the non-hydrostatic model presented here as well as its hydrostatic counterpart. For the sake of simplicity, we consider that the bottom is defined by the reference slope plane. In order to compute the simulation corresponding to system (16) in local coordinates we must set $\widetilde{b}_{loc}(x) = -\tan\theta\,(x - x_{end})$ and $b_{loc} = 0$. Conversely, in Cartesian coordinates we have to define $b_{Cart}(x) = -\tan\theta\,(x - x_{end})$, $\widetilde{b}_{Cart} = 0$, and write g instead of $g\cos\theta$ everywhere in system (16).

Let us remark that in this case the term $2\overline{q}\partial_X b$ in the non-hydrostatic model (16b) vanishes when the model is written in local coordinates, whereas it is equal to $-2\overline{q}\tan\theta$ in the Cartesian version of

the model. This behavior is very different if we compare with the hydrostatic model, where this term is always zero.

We shall analyze the influence of the choice of coordinates by considering a numerical test where the initial condition is well defined in both coordinate systems. We consider a computational domain given by the interval $[X_0, X_{end}]$. The initial condition is shown in Figure 4. We shall denote by $h_{loc}(X)$ and $h_{Cart}(x)$ the initial height function in local and Cartesian coordinates respectively. The initial height in Cartesian coordinates is given by

$$h_{Cart}(x) = \max\left(\eta_{ref} + \tan\theta\,(x - x_{end}), 0\right), \quad \text{for } x < x_{lim},$$

where η_{ref} is a reference level, x_{end} is the right boundary of the computational domain and x_{lim} is the initial front position.

In order to define the initial condition using local coordinates we use that $x = X\cos\theta$. Then, $X_{lim} = x_{lim}/\cos\theta$ is the initial position of the front position in local coordinates. We also use that the distance from $Y_b(X_{lim})$ to the reference level (vertically measured) is

$$H = \eta_{ref} + \sin\theta\,(X_{lim} - X_{end}),$$

which is the maximum height of the flow when considering Cartesian coordinates. Then, the maximum height of the initial condition defined in local coordinates is $\widehat{H} = H\cos\theta$, located in $\widehat{X} = X_{lim} - \widehat{H}\tan\theta$ (see figure 4b). Using this notation we can define the initial condition in local coordinates as follows:

$$h_{loc}(X) = \max(h_1(X), 0), \text{ with } h_1(X) = \begin{cases} y_1(X) = \max\left(\widehat{H} + \tan\theta\left(X - \widehat{X}\right), 0\right), & \text{if } X \le \widehat{X}, \\ y_2(X) = \max\left(\dfrac{1}{\tan\theta}\,(X_{lim} - X), 0\right), & \text{if } X > \widehat{X}. \end{cases}$$

In practice, we set the slope $\theta = 22^\circ$ and the computational domain (in local coordinates) $X \in [-0.5, 2.7]$, with 600 nodes. At initial time, the considered granular mass is at rest, the position of the front is assumed to be at $X = 0$, i.e. $X_{lim} = 0$, and the maximum (local) height is assumed to be $\widehat{H} = 0.14$ m. This is equivalent to consider a reference level $\eta_{ref} = 0.14/\cos\theta + x_{end}\tan\theta$ m.

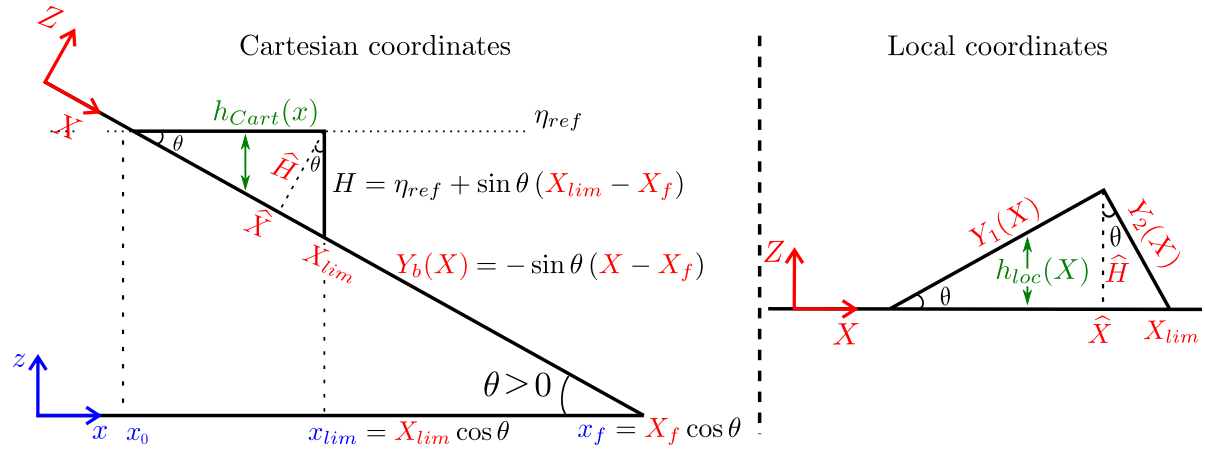

Figure 4: Sketch of the initial condition in Cartesian (blue) and local (red) coordinates.

Figure 5 shows the time evolution of hydrostatic (H) and non-hydrostatic (NH) local models in a local view, i.e. the flow thickness h is represented in the direction normal to the slope. The spreading of the granular mass simulated with the non-hydrostatic model is slower than with the hydrostatic model. As a result the front position is always located further downslope with the hydrostatic model, leading to significantly longer runout distance. Concretely, it is 11.8% bigger using the hydrostatic model. The maximum thickness of the flowing mass and of the deposit is also lower with the hydrostatic model, except at the very beginning of the flow. In Figure 6 we show the evolution of the flowing mass obtained with the hydrostatic and the non-hydrostatic models, in both coordinate systems. The simulations obtained with the hydrostatic model, both in local and Cartesian coordinates, are faster during the first instants than non-hydrostatic models. The non-hydrostatic model in Cartesian coordinates generate faster flows than the hydrostatic model in local coordinates for $t > 0.22$ s, approximately, leading to larger travelling distances of the granular front and consequently larger runout distance. From that time, the two models in Cartesian coordinates go further than the models in local coordinates. One of the outcome of this comparison is that the non-hydrostatic Cartesian model does not give the same results as the local hydrostatic model, contrary to what was assumed in [16]. This is also shown in Figure 7, where we see the time evolution of the granular front position. In the inset figure we see that the front position simulated with the non-hydrostatic (NH) model in Cartesian coordinates is slightly smaller than the one computed with the hydrostatic (H) model in local coordinates at short times while it is higher later on, as commented before. The final runout distance using the NH Cartesian model and the H local model are however similar as also assumed in [16]. Note also that the time change of the front position simulated with the NH local model exhibit a curvature change during the first instants as observed in laboratory experiments (Figure 9a of [37]) while is is not the case with hydrostatic models.

It is well-known that models in local coordinates are more appropriate than model in Cartesian coordinates, since local models compute the velocity in the direction tangent to the topography, which is the relevant direction for these dense granular flows. As a result, we will calculate the error made when using Cartesian coordinates instead of local coordinates. In the same way, we will chose as a

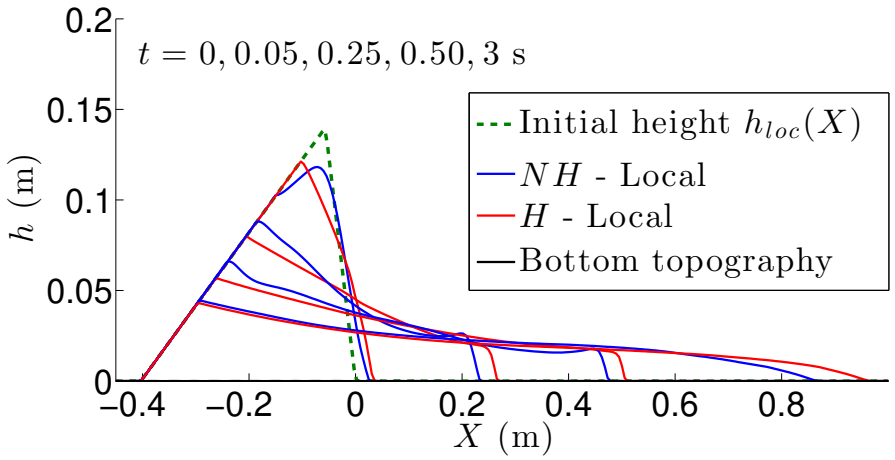

Figure 5: Deposits at different times of the hydrostatic (red lines) and the non-hydrostatic (blue lines) models computed in local coordinates. Dashed green line corresponds to the initial height.

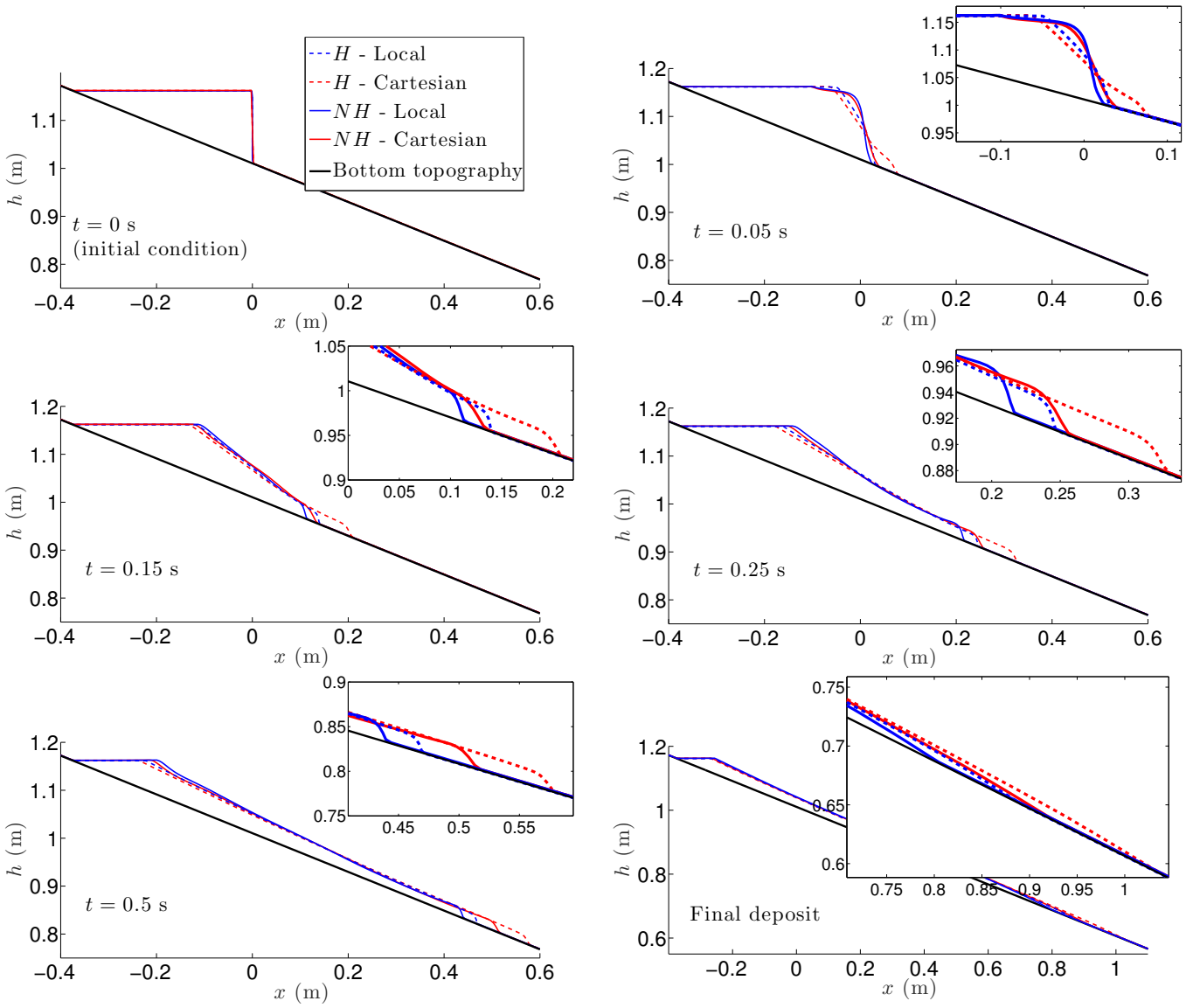

Figure 6: Thickness profiles of the granular mass flowing on a plane of inclination $\theta = 22^o$ at different times. Blue lines correspond to local models with hydrostatic (dashed) and non-hydrostatic (solid) pressure, while red lines are the solutions of Cartesian models with hydrostatic (dashed) and non-hydrostatic (solid) pressures. Inset figures show zooms of the front position.

reference the NH local model for which the shallow approximation and depth-integration is performed in the good direction and that includes some non-hydrostatic contribution.

In Figure 8 we show the relative error of the front position between the results obtained in Cartesian coordinates compared to the local coordinates for both the hydrostatic and non-hydrostatic models. We can observe that hydrostatic models are more dependent on the coordinate system. That is an expected behavior as fully 3D non-hydrostatic results are independent of the choice of the coordinate system. In Figure 9a and 9b we show relative errors on the front position and height along the domain computed

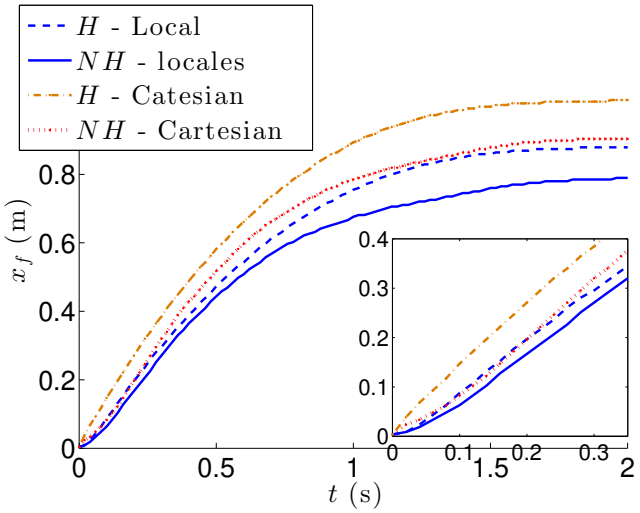

Figure 7: Time evolution of the granular front position x_f computed with the hydrostatic and the non-hydrostatic models in local coordinates (dashed and solid blue line, respectively), and the hydrostatic and the non-hydrostatic models in Cartesian coordinates (dot-dashed brown and dotted red line, respectively). Inset figure shows a zoom at short times.

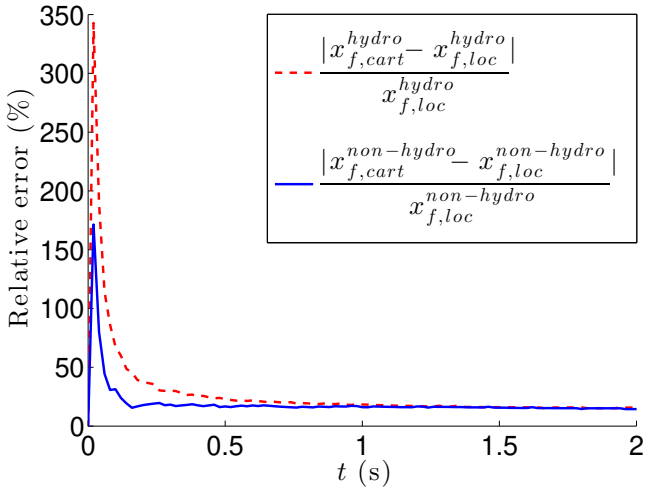

Figure 8: Time evolution of the relative errors of the front position x_f when changing the coordinates system. Dashed red line is the comparison for hydrostatic models, and solid blue line for non-hydrostatic models.

with the different models compared to the reference solution obtained with the NH local model with a finer mesh computed with 1200 nodes, i.e., $\widetilde{\Delta x} = \Delta x/2$. As expected, the errors corresponding to the solution of the Cartesian hydrostatic model are the biggest one, reaching 400% during the first instants up to 28% on the runout distance. These errors are lower when looking at the height along the domain.

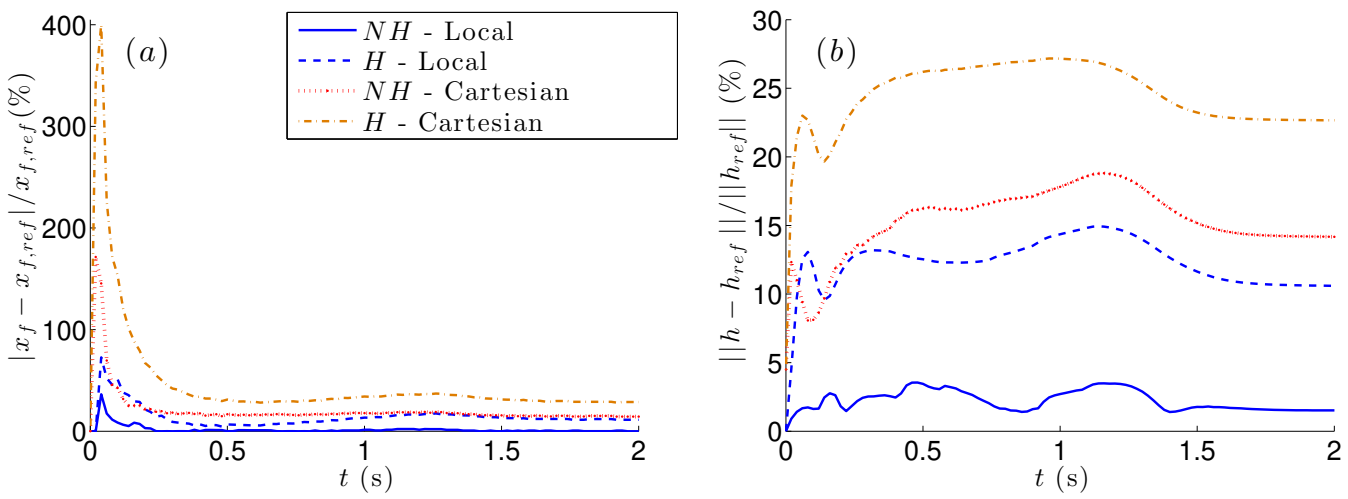

Figure 9: Time evolution of the relative errors computed with the local non-hydrostatic (NH) and the hydrostatic (H) models (solid and dashed blue lines respectively), the Cartesian NH and the H models (dotted red line and dot-dashed brown line respectively), taking as reference the results of the NH model in local coordinates with a finer mesh for (a) the front position x_f and (b) the granular mass thickness computed with L^2 norm.

This error is greater also for the H Cartesian model, being approximately 23% at final time, whereas it is 14% and 11%, approximately, for the NH Cartesian and H local models, respectively. This behavior is also seen in Figure 7. Finally, these figures show also the errors between the NH model with the coarse and finer meshes. We see a peak of this error at a very short time, but it is lower than 1% for $t > 0.22$ s, being zero (approximately 10^{-6}) for the runout distance. When looking at the height along the domain, this error is always lower than 3.5%, being approximately 1.5% at final time. We can conclude that hydrostatic models in Cartesian coordinates predict a much too long runout distance. Nevertheless, and interestingly, the Cartesian non-hydrostatic model and the local hydrostatic model give similar deposits even though the dynamics is different, as shown in figures 9 and 7. This partly supports the assumption of [16] but only for the deposit. Indeed, these authors proposed a hydrostatic model in Cartesian coordinates with a correction of the pressure accounting for an approximation of the vertical acceleration. They showed that their model produces similar results to the ones obtained with the hydrostatic local model for the analytical solution of a dam break problem (see their Figure 4b).

This last result motivates the next test, where these two models (H-local and NH-Cartesian) are compared in a more general case, with a more complex topography.

4.4 Hydrostatic local model vs Non-hydrostatic Cartesian model

The goal of this test is to show a qualitative comparison of the hydrostatic local and the non-hydrostatic Cartesian model for flows on a complex topography. We consider here a granular mass, with the same rheological properties (see Table 1) as in previous test, in the computational domain $[-3, 3]$. In this case we take 640 nodes for the horizontal discretization. The topography, in Cartesian coordinates, is

given by $\widetilde{b}_{Cart} = 0$ and

$$b_{Cart}(x) = 1 - \tanh(x) + 0.3e^{-10(x-1)^2} + 0.5e^{-10(x-3)^2}, \tag{34}$$

and the initial height is

$$h_{Cart}(x) = \max(\eta(x) - b_{Cart}(x), 0), \quad \text{with} \quad \eta(x) = \begin{cases} y_0 - 1 + e^{-0.5(x-x_0)^8}, & \text{if } x \leq 0, \\ 0, & \text{otherwise,} \end{cases}$$

with $x_0 = -1.53$ m and $y_0 = 1.91$ m.

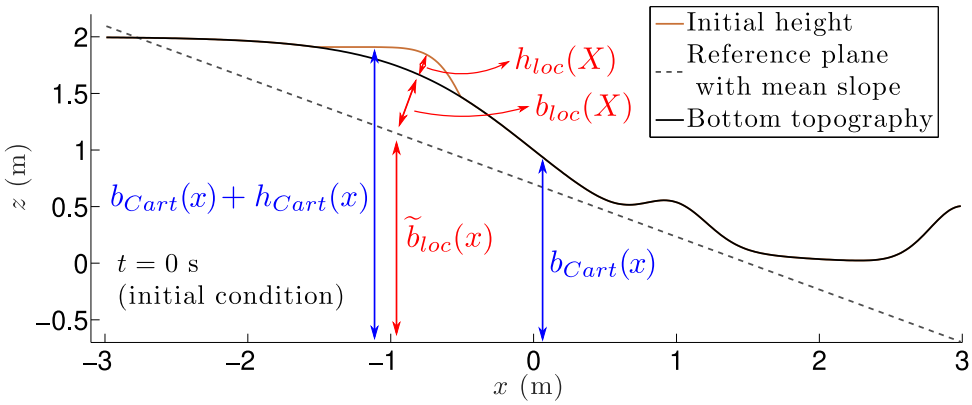

Figure 10: Initial height (solid red line), bottom topography (solid black line) and reference plane with the mean slope used for the local model (dashed gray line).

Defining this initial configuration in local coordinates is not a simple task. First, a reference plane $\widetilde{b}_{loc}(x)$, whose slope is the mean slope of the topography, is defined. In our case, $\widetilde{b}_{loc}(x) = -0.7 - \tan(25°)(x-3)$. Then, the topography $b_{loc}(X)$ is defined as the distance from $\widetilde{b}_{loc}(x)$ to $b_{loc}(X)$, measured in the normal direction to the reference plane $\widetilde{b}_{loc}$ (see Figure 10). Analogously, the height $h_{loc}(X)$ is the distance from $b_{loc}(X)$ to $h_{loc}(X)$. The granular mass is supposed to be initially at rest. After some time the grains stop, leading to three separate regions of material at rest.

Figure 11 shows the height at times 0.5, 1.5, 2.5 s and the final deposit. We show the results of the non-hydrostatic local, the hydrostatic local, the hydrostatic Cartesian and the non-hydrostatic Cartesian models. We see that the hydrostatic Cartesian model is the fastest one, and the non-hydrostatic local model is the slowest one as observed previously. We also see that the results of the hydrostatic local model and the non-hydrostatic Cartesian models are close for $t > 2.3$ s. Actually, the final deposits computed with both models are similar even though the dynamics differ. Moreover, the solution of the hydrostatic Cartesian model widely differs from the other models.

These results confirm that the hydrostatic local model and the non-hydrostatic Cartesian model produce similar deposits even though the dynamics is different, but not too different in this test. Moreover, in view of the results, the non-hydrostatic Cartesian model proposed here is an improvement of the model introduced in [16], in the sense that our model computes the vertical acceleration while their model uses an estimate of this acceleration by taking the average of the vertical velocity deduced from the free surface and bottom boundary condition.

In the rest of the paper, we shall only use local models.

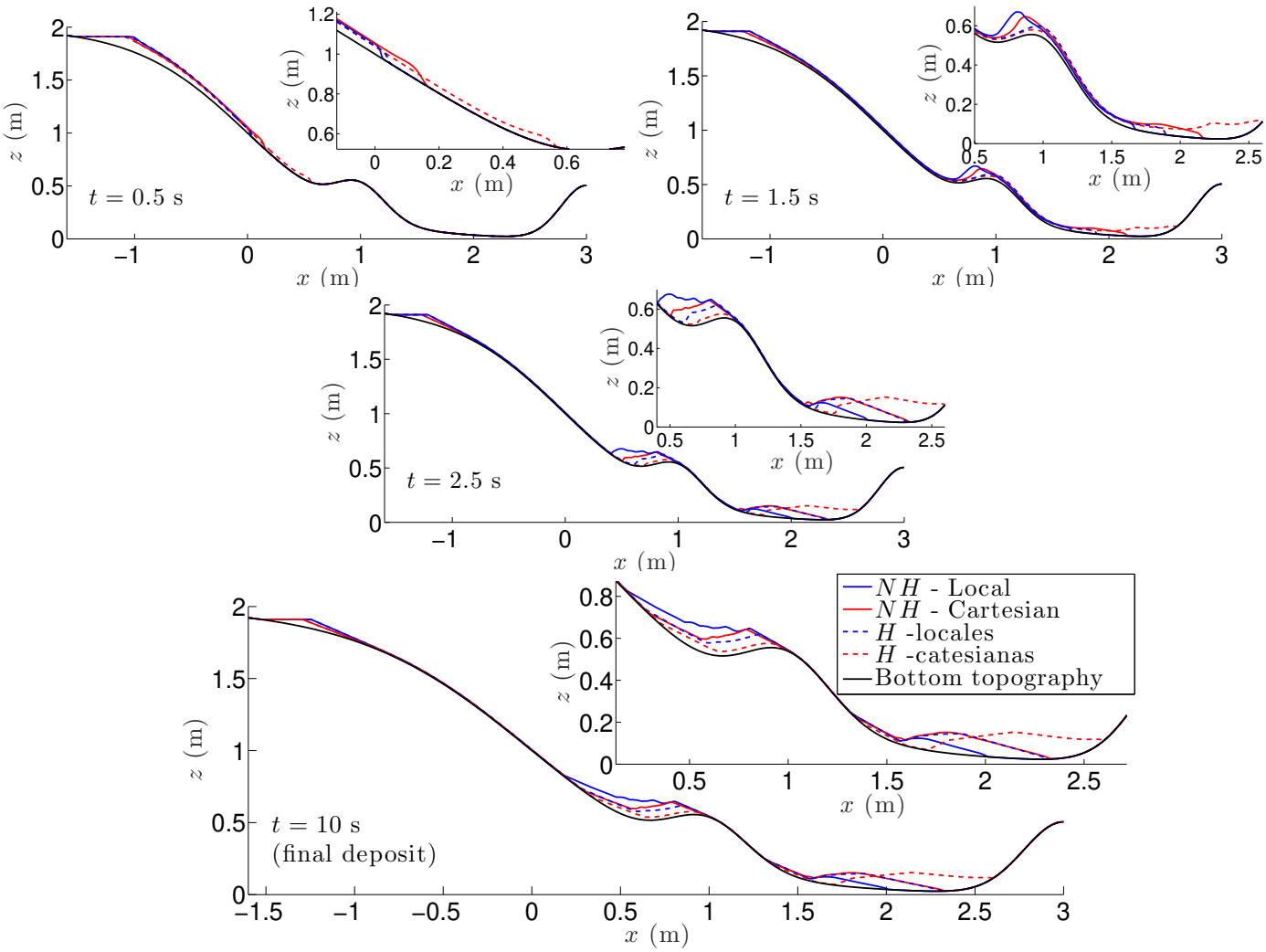

Figure 11: Height of the flowing mass at different times. Blue lines correspond to local models with non-hydrostatic (solid) and hydrostatic (dashed) pressure, while red lines are the solutions of Cartesian models with hydrostatic (dashed) and non-hydrostatic (solid) pressures. Inset figures show zooms of the front position.

4.5 Comparison with experimental granular collapses

In this section we compare the results of the hydrostatic and the non-hydrostatic models with experimental data detailed in [37]. In these experiments, we have a granular column of height $h_0 = 14$ cm and length $L = 20$ cm, which is initially confined in a tank. The gate is opened so that the material is released from rest and flows over an inclined plane with slope $\theta \geq 0$. We consider here five different slopes, $\theta = 0°, 9.78°, 16°, 19°$ and $22°$. The bed is made of the same particles glued on it.

The computational domain is $[-0.2, 3]$ m with 640 points and the initial height is given by

$$h_0(x) = \begin{cases} 0.14 & \text{if } x \leq 0; \\ 0 & \text{otherwise.} \end{cases}$$

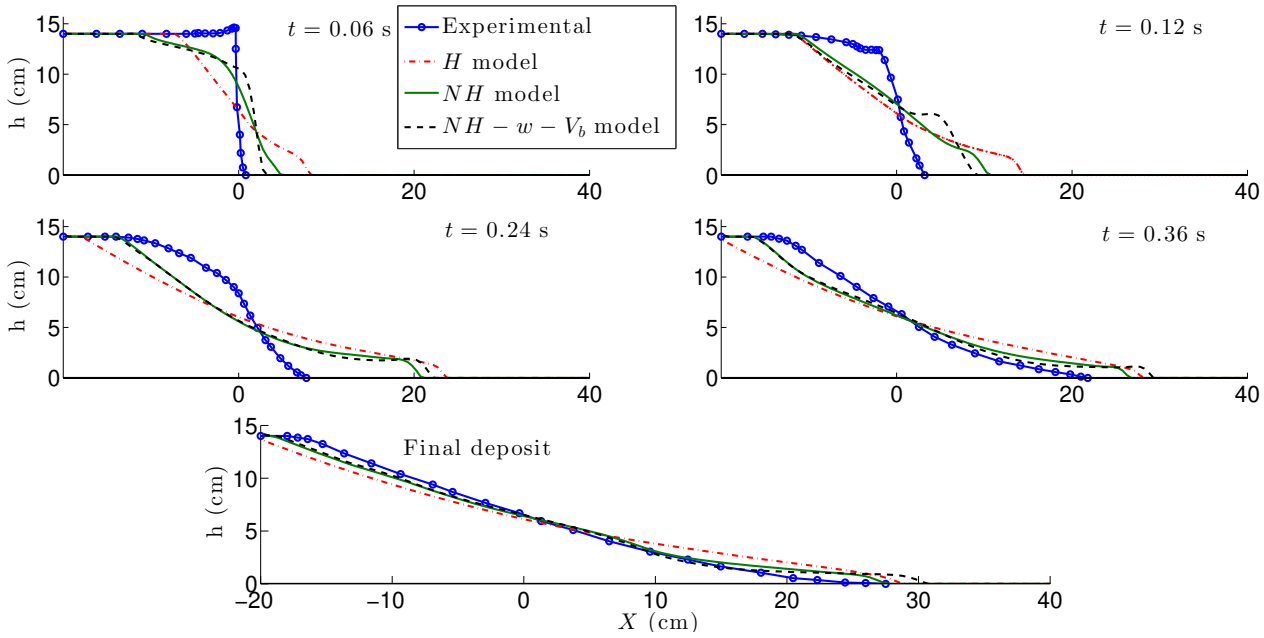

Figure 12: Time evolution of the granular mass with slope $\theta = 0°$, for the laboratory experiments (solid-circle blue line), the hydrostatic model (dot-dashed red line), the non-hydrostatic model (solid green line) and the non-hydrostatic model with gate effect (dashed black line).

Let us remark that the gate removal induces a vertical velocity to the material that is located near the front, in contact with the gate. This cannot be reproduced by hydrostatic models, but using non-hydrostatic models we can impose the initial vertical velocity induced by the gate removal. This is an advantage of the non-hydrostatic model.

To do that, we consider an initial vertical velocity defined by

$$W_b(x) = \begin{cases} V_b & \text{if } -0.025 < x < 0; \\ 0 & \text{otherwise,} \end{cases} \tag{35}$$

where V_b, is the estimated velocity at which the gate is removed. In the experiment it is estimated that $V_b = 2.3\ m/s$ (see [27]). Imposing this velocity to the grains is different to what was done in [27] where they prescribed this velocity to a friction-free moving wall confining the domain and not directly to the grains. What we do here lead to overestimate the grain velocity because their motion should be slower than the uplifting velocity of the gate. This, together with the fact that they solved the full 2D Navier-Stokes system, allows them to obtain better results. However, the computational effort is much bigger. In order to show how the non-hydrostatic model could be used to study the effect of the gate, we also have performed these numerical tests using this initial vertical velocity, which will be analyzed later.

Figures 12, 13, 14, 15 and 16 show the thickness of the granular mass at different times, and the final deposit obtained with the hydrostatic and the non-hydrostatic model for slopes $\theta = 0°, 9.78°, 16°, 19°$ and $22°$. We shall in particular focus on the solutions at short times. The reason is that when the gate is opened and the material starts to flow, the non-hydrostatic effects are strong because the mass is not shallow, involving strong gradients of the free surface. The non-hydrostatic effects decrease as the mass

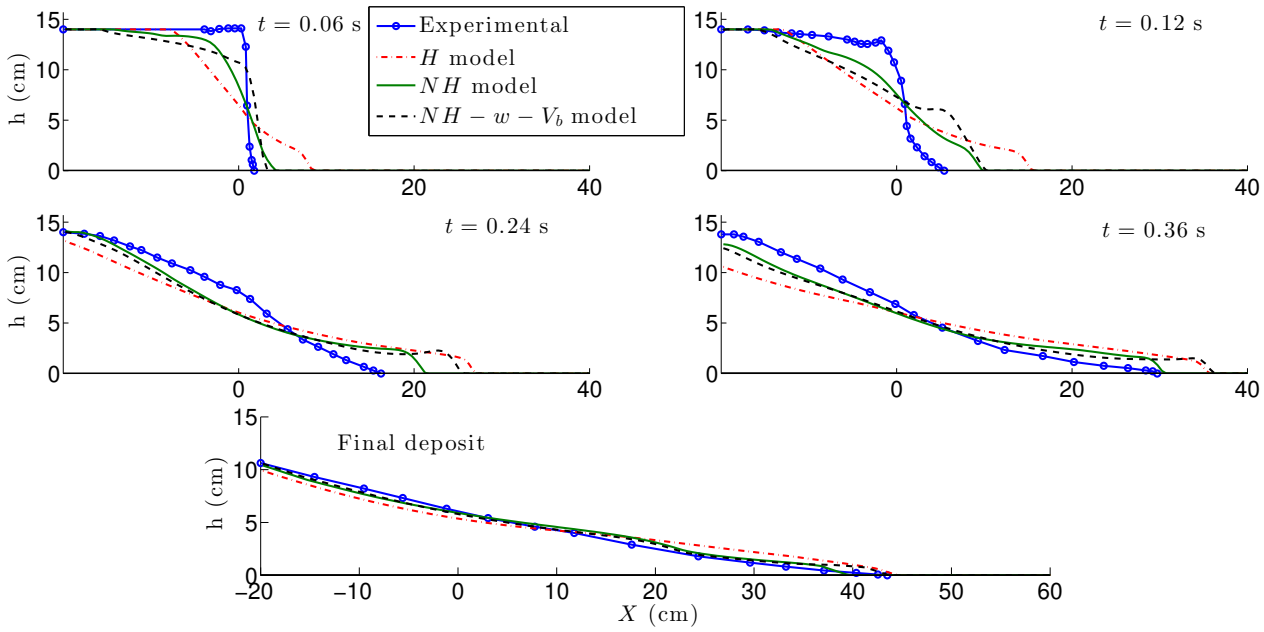

Figure 13: Time evolution of the granular mass over a plane with slope $\theta = 9.78°$, for the laboratory experiments (solid-circle blue line), the hydrostatic model (dot-dashed red line), the non-hydrostatic model (solid green line) and the non-hydrostatic model with gate effect (dashed black line).

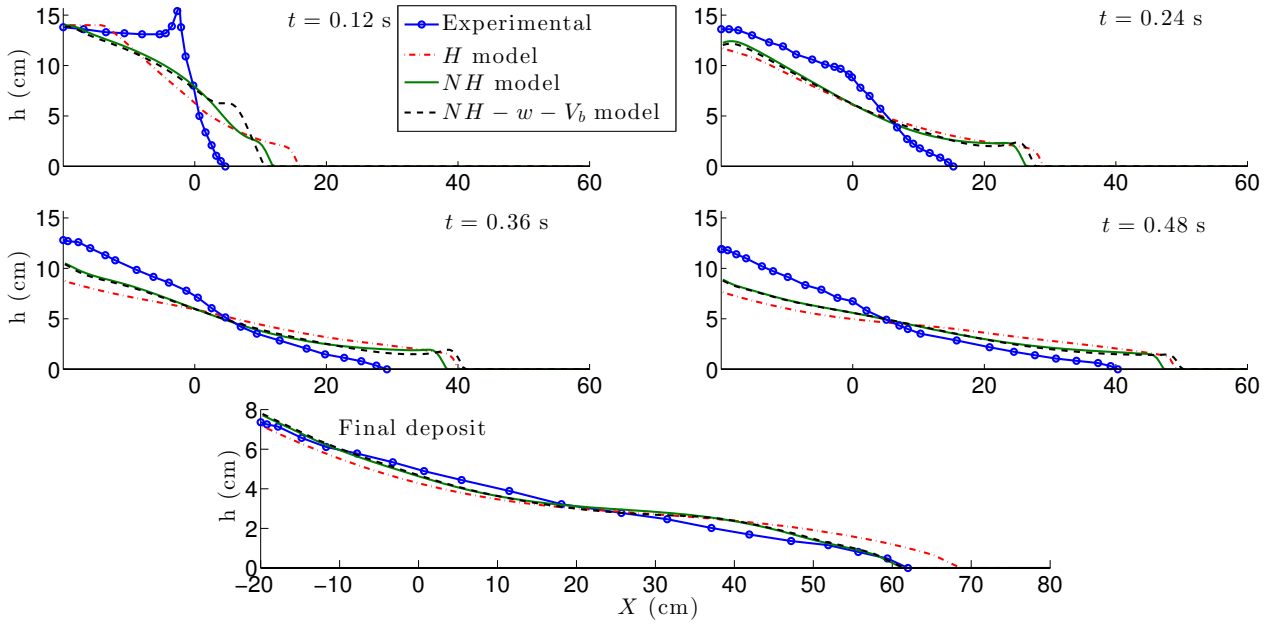

Figure 14: Time evolution of the granular mass over a plane with slope $\theta = 16°$, for the laboratory experiments (solid-circle blue line), the hydrostatic model (dot-dashed red line), the non-hydrostatic model (solid green line) and the non-hydrostatic model with gate effect (dashed black line).

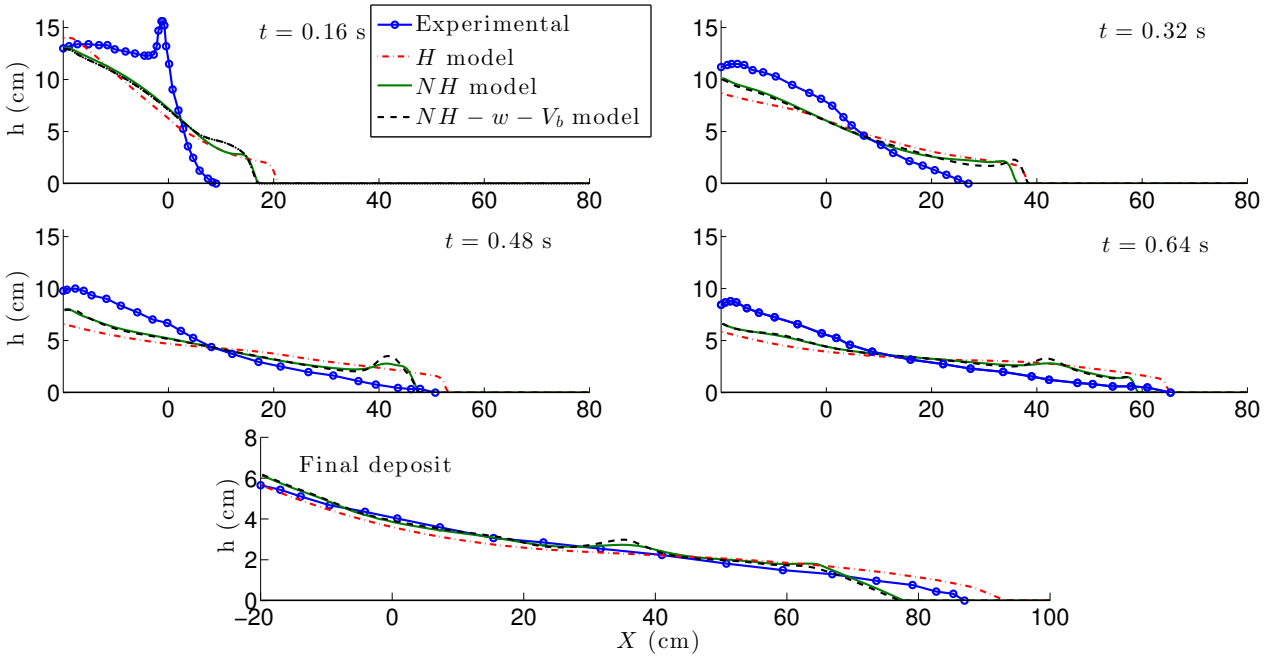

Figure 15: Time evolution of the granular mass over a plane with slope $\theta = 19°$, for the laboratory experiments (solid-circle blue line), the hydrostatic model (dot-dashed red line), the non-hydrostatic model (solid green line) and the non-hydrostatic model with gate effect (dashed black line).

spreads and gets closer to a shallow layer. One of the known consequences of these non-hydrostatic effects is that the granular mass does not start moving as fast as when using models based on the hydrostatic assumption (see e.g. [38], [22]).

We indeed observe that the solution of the non-hydrostatic model is slower and more accurate than the solution obtained with the hydrostatic model in all the studied configurations, as detailed below. The final deposits obtained with the non-hydrostatic model are in good agreement with the experiments, in particular for $\theta = 9.78°, 16°$ (see figures 13, 14).

We see this behavior even more clearly in Figure 17, where the position of the front at different times is represented. It is observed that the front position computed with the non-hydrostatic model is closer to the one obtained in the laboratory experiments up to a certain time, even though at the final instants the front position simulated with the NH model may be less accurate than with the H model as also observed on Figure 17a, showing the final runout r_f as function of the slope. Indeed in figures 17a,17c,17e the experimental runouts for $\theta = 9.78°$ and $\theta = 19°$ are closer to the hydrostatic model than to the non-hydrostatic one. Nevertheless, for $\theta = 9.78°$, looking at the final deposit in Figure 13, we see that the experimental front has a very small thickness. If we do not consider these very small thicknesses, the observed runout distance gets closer to the NH results than to the H simulations. For $\theta = 19°$, even though the runout distance is underestimated with the NH model, the whole granular thickness is better approximated with the NH model (see Figure 15), as explained below and as represented in Figure 18.

In order to quantify how accurately the models reproduce laboratory experiments when including non-hydrostatic terms, we represent in Figure 18 the relative error on the mass thickness between the simulation and the experiments averaged over all the domain at a given time. This error is computed

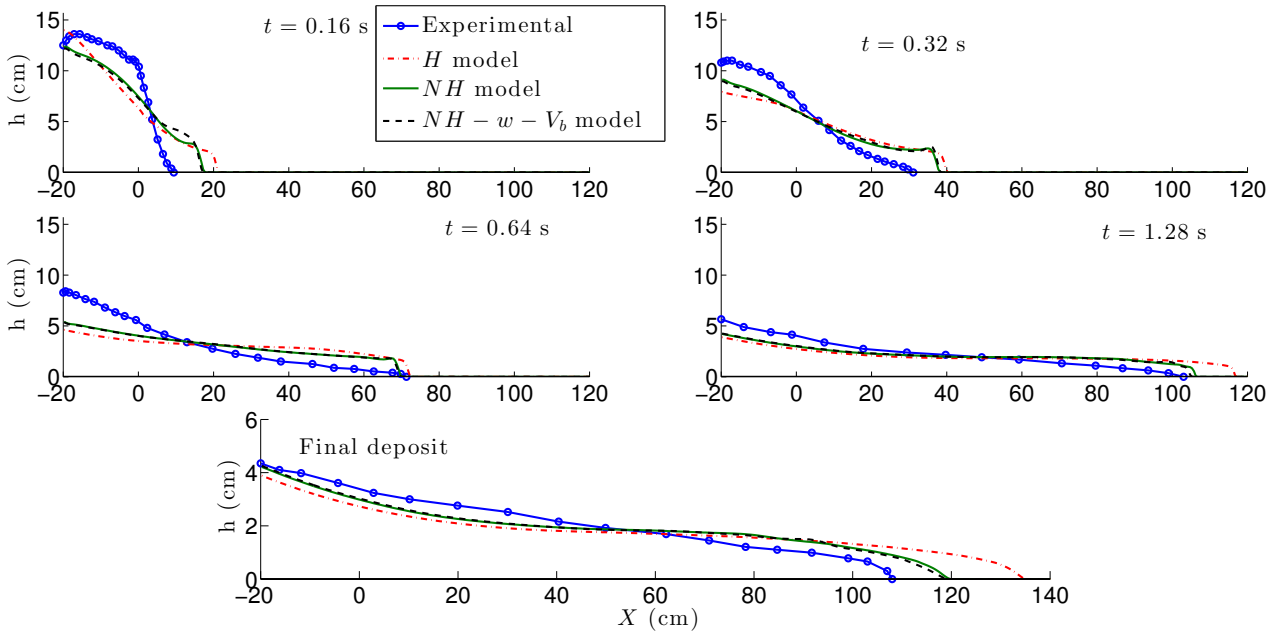

Figure 16: Time evolution of the granular mass over a plane with slope $\theta = 22°$, for the laboratory experiments (solid-circle blue line), the hydrostatic model (dot-dashed red line), the non-hydrostatic model (solid green line) and the non-hydrostatic model with gate effect (dashed black line).

at a given short time t_{ini} (chosen as a time for which the flow is initialized and we have experimental data) and at the final time t_f. We see that the error obtained with the non-hydrostatic model is smaller than the one obtained with the hydrostatic model for all slopes and for both the short and the final times. In particular, for $\theta = 9.78°$ at final time, the error computed with the non-hydrostatic model is 7% approximately, whereas this error is greater than 15% with the hydrostatic model. Figure 18 also shows that the error is smaller at the final time than at the short time. One of the source of the error is related to the depth-averaged process as shown in [22, 23]. In particular the rounded shape of the front obtained in the simulations disappears when multi-layer models are used, i. e. when no depth-averaging is performed (compare e. g. Figure 16 of the present paper to Figure 14 of [22]). Note that the error seems to increase with increasing slope. This may be due to wall effects that are more and more important as the slope angle increases as shown in [40].

In the figures, we see a small peak in the experiments at very short times. This results from the gate opening when releasing the granular material. Figures 12, 13, 14, 15, 16 and 17 also show the results obtained when imposing an initial vertical velocity $w_0(x)$ at the front position where the gate is located. We see that the results obtained with $w_0(x) \neq 0$ are similar to the non-hydrostatic model starting from rest ($w_0(x) = 0$) at large times, whereas they differ for short times. We also see in Figure 17 that the evolution of the front position improves for short times when including the vertical velocity mimicking the gate removal, while this has almost no effect at final times. Moreover, we see that the influence of the gate is stronger for small slopes ($\theta = 0°, 9.78°$) than for larger slopes ($\theta = 16°, 19°, 22°$). The results obtained here differ from those of [27], which used the full 2D Navier-Stokes equations (i. e. fully non-hydrostatic pressure) and described the gate as a moving boundary without friction. Indeed, in their simulation, gate effects make the front propagate more slowly at the beginning as observed here. However, their runout distance is independent of the gate, in contrary to what is obtained here

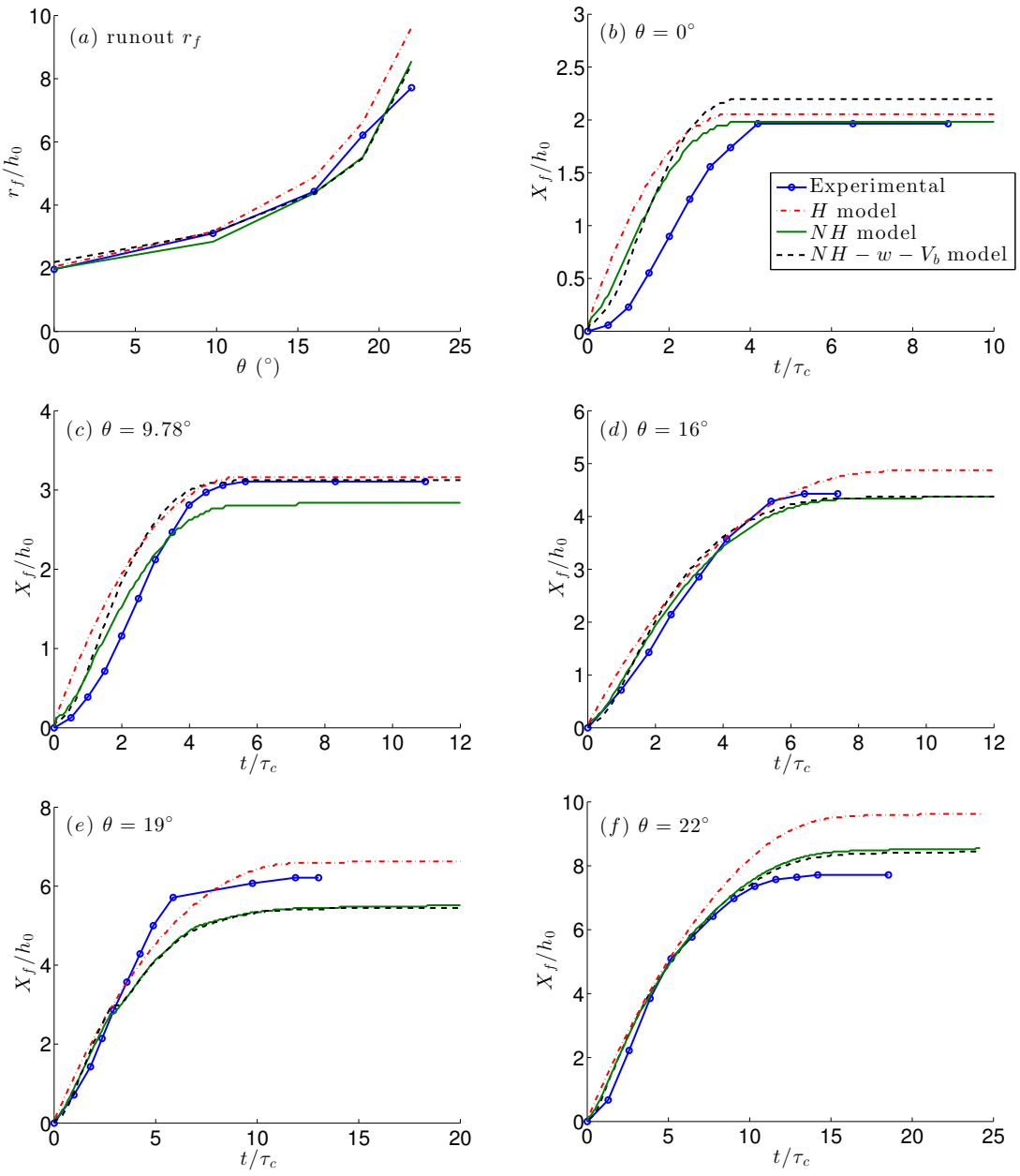

Figure 17: (a) Normalized runout for all the slopes; (b)-(f) time evolution of the normalized position of the front computed with the hydrostatic model (dot-dashed red line), the non-hydrostatic model (solid green line), the non-hydrostatic model with the effect of the gate at initial times (dashed black line), and experimental data (solid-circle blue lines). $h_0 = 0.14$ m and $\tau_c = \sqrt{h_0/(g\cos\theta)}$ s.

for $\theta = 0°$ and $\theta = 9.78°$ (see figures 12 and 13, respectively).

Figure 19 shows the velocity of the front for all the slopes. In the experiments we see that the velocity grows up at the beginning, and it decreases after an intermediate time, describing thus a

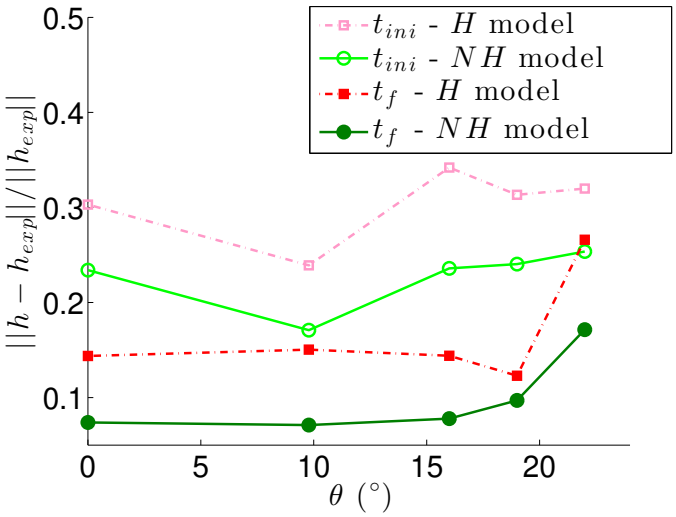

Figure 18: Relative errors of the height along the domain computed with the hydrostatic (dot-dashed lines) and non-hydrostatic (solid lines) models. Filled-symbols lines correspond to the errors at final times $t_f = 1.06\,(0°),\ 1.32\,(9.78°),\ 1.62\,(16°),\ 1.5\,(19°),\ 2.3\,(22°)$ s, while empty-symbols lines are the errors at time $t_{ini} = 0.24\,(0°, 9.78°), 0.36\,(16°),\ 0.32\,(19°, 22°)$ s.

parabolic profile. This behavior is reproduced with the non-hydrostatic model. On the contrary, the front velocity computed with the hydrostatic model starts from its maximum value and then decreases. This is an important improvement of NH models. Indeed, despite of being a simple model which neglects the first order contribution of the non-hydrostatic pressure (11), the shape of the front velocity is much better reproduced than with hydrostatic models.

In Figure 19 we also see that the front velocity is smaller during the first instants for the model including an initial vertical velocity $w_0 \neq 0$. Next, its growth is faster and the maximum velocity of the front is larger than the one computed with $w_0 = 0$. Interestingly, the maximum velocity is reached at similar times for both models.

Figure 20 shows the time evolution of the maximum vertical velocity, which is reached close to the front, for the smallest and biggest studied slopes $\theta = 0°, 22°$. This velocity, when computed with the hydrostatic model, is bigger than with the non-hydrostatic model. This figure also shows the differences of estimated potential energy (gh) and kinetic energy (V^2) between the hydrostatic and the non-hydrostatic model, for all the slopes. In order to approximate the kinetic energy (V^2) we use the downslope velocity u or the velocity vector (u, w). For each case, we take the maximum on time, and the maximum or the average on space of V^2. Next, we compute the (relative) difference between the values computed with the hydrostatic and the non-hydrostatic model for a fixed slope. We see that, for small slopes, the difference between the models is significantly greater for the kinetic energy than for the potential one (which also represents the differences on the height), and these are of the same order of magnitude for all the slopes. However, the difference of the kinetic energy are greater for small values of the slope. We could conclude that the difference between the two models is bigger for small slopes.

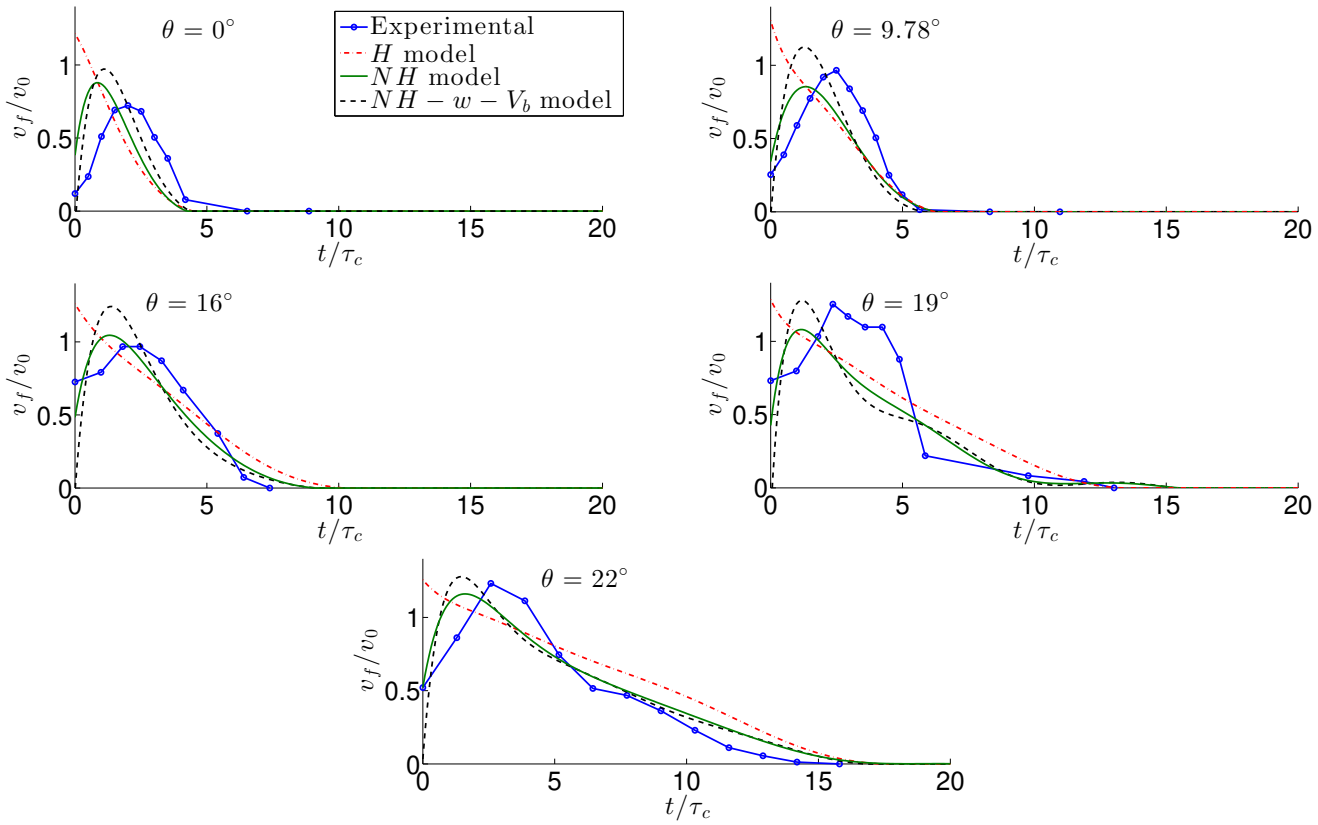

Figure 19: Time evolution of the normalized velocity of the front computed with the hydrostatic model (dot-dashed red line), the non-hydrostatic model (solid green line), the non-hydrostatic model with the effect of the gate at initial times (dashed black line), and experimental data (solid-circle blue lines). $h_0 = 0.14$ m, $v_0 = \sqrt{h_0 g \cos\theta}$ m/s and $\tau_c = \sqrt{h_0/(g\cos\theta)}$ s.

5 Conclusions

In this work a non-hydrostatic depth-averaged model for dry granular flows has been proposed. The model considers a friction term based on the $\mu(I)$ rheology, where the friction coefficient depends on both the pressure (hydrostatic and non-hydrostatic) and the velocity. For the sake of simplicity, we assume that the non-hydrostatic pressure has a linear profile. For other profiles, the system would have extra unknowns and equations resulting in more complexity from the computational point of view (see e.g. [24]).

The proposed model notably improves the results of hydrostatic models, in particular when comparing our results with dam break laboratory experiments. The model can be seen as a correction of classical Savage-Hutter type models with a $\mu(I)$ friction law. Its numerical discretization can also be adapted for any existing hydrostatic code by adding two additional steps to the numerical scheme. In addition, we have proven that the proposed scheme is well-balanced in the sense that it preserves discrete steady states whose slope is lower than the angle of repose. In particular, it is exactly well-balanced for solution with constant slope verifying that.

We performed numerical tests to study the order of convergence and the well-balanced properties

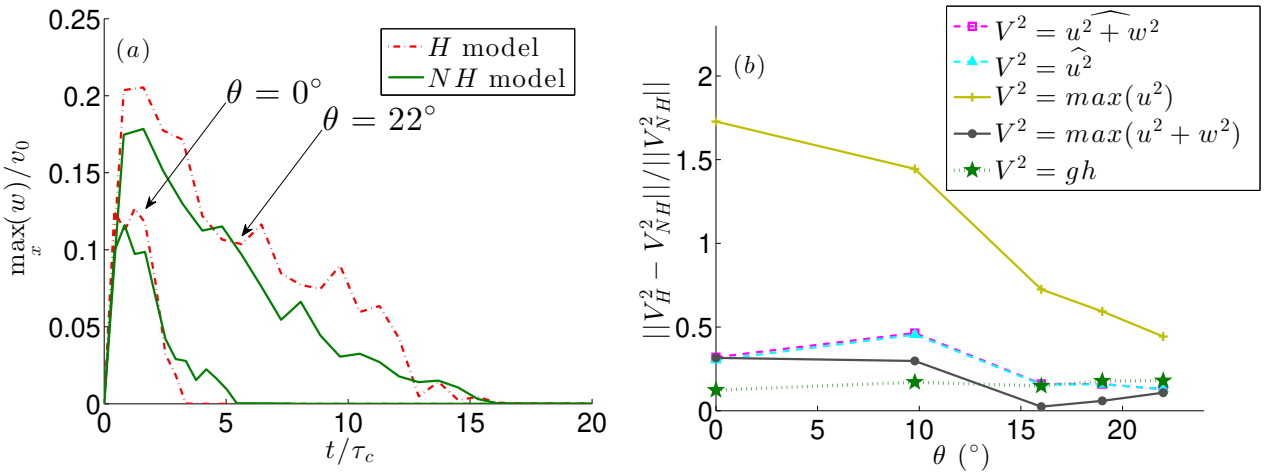

Figure 20: (a) Time evolution of the maximum of the vertical velocity for $\theta = 0°, 22°$ computed with the hydrostatic (dot-dashed red lines) and the non-hydrostatic (solid green lines) model. $h_0 = 0.14$ m, $v_0 = \sqrt{h_0 g \cos\theta}$ m/s and $\tau_c = \sqrt{h_0/(g\cos\theta)}$ s. (b) Maximum on time of the differences of estimations of the energy between hydrostatic and non-hydrostatic models for all the slopes. $\max(\cdot) = \max_{t,x}(\cdot)$ and $\widehat{(\cdot)} = \max_t\left(\sum_{1\le i\le N}(\cdot)/N\right)$.

of the numerical scheme. We have also analyzed the influence of the coordinate system (Cartesian or local) for the hydrostatic and non-hydrostatic model. The non-hydrostatic models (both Cartesian and local) predict a slower motion of the granular front at the beginning. However, the front positions computed with both Cartesian models are longer after some time, as expected. It is due to the fact that Cartesian model use the horizontal velocity instead of the velocity tangent to the topography. The biggest differences between the NH local model with a finer mesh and the H local, NH Cartesian, and H Cartesian models are found for short times (see Figure 9a). Namely, the maximum of this difference is around 400% for the H Cartesian and 170% for the NH Cartesian models at time $t = 0.03$ s, whereas it is 72% for the H local model at $t = 0.04$ s.

In addition, the deposits obtained with the local hydrostatic model and the Cartesian non-hydrostatic models are similar even though the dynamics differs. These results partly support the assumption made by [16] where a hydrostatic Cartesian model with a correction of the pressure based on an approximation of the vertical acceleration is proposed with the aim to avoid working in local curvilinear coordinates. In that sense, our non-hydrostatic Cartesian model is an improvement of the one proposed in [16], since the vertical acceleration is computed and not estimated. This has been studied in test 4.4, where a complex topography has been used, obtaining similar conclusions. We have also observed that the non-hydrostatic models are less dependent on the coordinate system than the hydrostatic models, which is also an expected result.

Comparisons have been made with laboratory experiments, and also with a hydrostatic model (Savage-Hutter model with a $\mu(I)$ friction coefficient). The non-hydrostatic model improves the results of the hydrostatic one, in particular at short times, which is clear by looking at the time evolution of the position of the front. The shape of the flowing mass and of the deposit is also always closer to the experiments when using non-hydrostatic models. The importance of non-hydrostatic terms is higher for smaller slopes, as expected. The approximation of the front position is also improved when using the non-hydrostatic model, making it possible to slow down the too fast propagation of the front

observed in hydrostatic models ([38], and figure 9 of [37]. Moreover, we have shown that the thickness distribution is always better reproduced by the NH model compared to the H model, both at short and final times. For example, as shown in Figure 18, for $\theta \leq 16^\circ$ ($\theta = 22^\circ$, respectively) the relative error between simulated and observed thickness distribution is around 15% for the H model while it is approximately 7% for the NH model (27% and 17%, respectively).

By using this non-hydrostatic model we may impose a vertical velocity at initial time, which mimics the effect of the gate opening. The gate opening has a strong influence on the dynamics at short times. However, this has almost no effect on the final deposit as shown by [27], where they use the full Navier-Stokes equations and impose the movement of the gate as a moving wall boundary condition. With the model proposed here, we also obtain this gate effect at initial time for small slopes ($\theta = 0^\circ, 9.78^\circ$), whereas the results are almost identical for large slopes ($\theta = 16^\circ, 19^\circ, 22^\circ$).

An important result is the fact that our non-hydrostatic model predicts the parabolic shape of the velocity of the front as a function of time, as observed in the experiments. This is not reproduced at all by hydrostatic models where the velocity of the front starts from its maximum. Such improvement is obtained even though our model is only weakly non-hydrostatic, in the sense that we do not take into account the contribution of the stress tensor in the non-hydrostatic pressure. In the future it would be interesting to include viscous terms, as well as the extension of the presented model using a vertical discretization such as the multilayer approach, which gave promising results for hydrostatic granular flows (see [22, 23]) and also for non-hydrostatic inviscid fluids [24]. A further study on how to implement a breaking mechanism for the model studied here will be interesting as well.

Acknowledgements

This research has been partially supported by the Spanish Government and FEDER through the research projects MTM2015-70490-C2-2-R and RTI2018-096064-B-C22, and by the ERC contract ERC-CG-2013-PE10-617472 SLIDEQUAKES. The authors would like to thank Cipriano Escalante for the interesting discussions related to this work.

References

[1] B. Andreotti, Y. Forterre, and O. Pouliquen. *Granular Media: Between Fluid and Solid*. Cambridge University Press, 2013.

[2] E. Audusse, F. Bouchut, M. Bristeau, R. Klein, and B. Perthame. A fast and stable well-balanced scheme with hydrostatic reconstruction for shallow water flows. *SIAM Journal on Scientific Computing*, 25(6):2050–2065, 2004.

[3] J. L. Baker, T. Barker, and J. M. N. T. Gray. A two-dimensional depth-averaged μ(I)-rheology for dense granular avalanches. *Journal of Fluid Mechanics*, 787:367–395, 1 2016.

[4] F. Bouchut. *Nonlinear Stability of Finite Volume Methods for Hyperbolic Conservation Laws: And Well-Balanced Schemes for Sources*. Springer Science & Business Media, 2004.

[5] F. Bouchut, E. D. Fernández-Nieto, A. Mangeney, and G. Narbona-Reina. A two-phase two-layer model for fluidized granular flows with dilatancy effects. *Journal of Fluid Mechanics*, 801:166–221, August 2016.

[6] F. Bouchut, I. Ionescu, and A. Mangeney. An analytic approach for the evolution of the static-flowing interface in viscoplastic granular flows. *Communications in Mathematical Sciences*, 14(8):2101–2126, 2016.

[7] F. Bouchut and M. Westdickenberg. Gravity driven shallow water models for arbitrary topography. *Communications in Mathematical Sciences*, 2(3):359–389, 09 2004.

[8] Mehdi Bouzid, Martin Trulsson, Philippe Claudin, Eric Clément, and Bruno Andreotti. Nonlocal rheology of granular flows across yield conditions. *Physical Review Letters*, 111(23), dec 2013.

[9] M.-O. Bristeau, A. Mangeney, J. Sainte-Marie, and N. Seguin. An energy-consistent depth-averaged Euler system: Derivation and properties. *Discrete and Continuous Dynamical Systems Series B*, 20(4):961–988, 2015.

[10] M. Brunet, L. Moretti, A. Le Friant, A. Mangeney, E. D. Fernández Nieto, and F. Bouchut. Numerical simulation of the 30–45 ka debris avalanche flow of Montagne Pelée volcano, Martinique: from volcano flank collapse to submarine emplacement. *Natural Hazards*, 87(2):1189–1222, apr 2017.

[11] M. J. Castro, J. M. González-Vida, and C. Parés. Numerical treatment of wet/dry fronts in shallow flows with a modified Roe scheme. *Mathematical Models and Methods in Applied Sciences*, 16(06):897–931, jun 2006.

[12] M. J. Castro Díaz and E. D. Fernández-Nieto. A class of computationally fast first order finite volume solvers: PVM methods. *SIAM Journal on Scientific Computing*, 34(4):A2173–A2196, 2012.

[13] V. Casulli. A semi-implicit finite difference method for non-hydrostatic free-surface flows. *International Journal for Numerical Methods in Fluids*, 30(4):425–440, jun 1999.

[14] R. Delannay, A. Valance, A. Mangeney, O. Roche, and P. Richard. Granular and particle-laden flows: from laboratory experiments to field observations. *Journal of Physics D: Applied Physics*, 50(5):053001, 2017.

[15] J.M. Delgado-Sánchez, F. Bouchut, E.D. Fernández-Nieto, A. Mangeney, and G. Narbona-Reina. A two-layer shallow flow model with two axes of integration, well-balanced discretization and application to submarine avalanches. *Journal of Computational Physics*, 406:109186, apr 2020.

[16] R.P. Denlinger and R.M. Iverson. Granular avalanches across irregular three-dimensional terrain: 1. Theory and computation. *Journal of Geophysical Research: Earth Surface*, 109(F1), mar 2004.

[17] A. N. Edwards and J. M. N. T. Gray. Erosion-deposition waves in shallow granular free-surface flows. *Journal of Fluid Mechanics*, 762:35–67, January 2015.

[18] C. Escalante, T. Morales de Luna, and M.J. Castro. Non-Hydrostatic Pressure Shallow Flows: GPU Implementation Using Finite Volume and Finite Difference Scheme. *Applied Mathematics and Computation*, (338):631–659, 2018.

[19] C. Escalante and T. Morales de Luna. A general non-hydrostatic hyperbolic formulation for boussinesq dispersive shallow flows and its numerical approximation. *Journal of Scientific Computing*, 83(3), jun 2020.

[20] E. D. Fernández-Nieto, F. Bouchut, D. Bresch, M. J. Castro Díaz, and A. Mangeney. A new Savage-Hutter type model for submarine avalanches and generated tsunami. *Journal of Computational Physics*, 227(16):7720–7754, 2008.

[21] E. D. Fernández-Nieto, J. M. Gallardo, and P. Vigneaux. Efficient numerical schemes for viscoplastic avalanches. Part 1: The 1D case. *Journal of Computational Physics*, 264:55–90, may 2014.

[22] E. D. Fernández-Nieto, J. Garres-Díaz, A. Mangeney, and G. Narbona-Reina. A multilayer shallow model for dry granular flows with the $\mu(I)$ rheology: Application to granular collapse on erodible beds. *Journal of Fluid Mechanics*, 798:643–681, 2016.

[23] E. D. Fernández-Nieto, J. Garres-Díaz, A. Mangeney, and G. Narbona-Reina. 2D granular flows with the $\mu(I)$ rheology and side walls friction: a well-balanced multilayer discretization. *Journal of Computational Physics*, 356:192–219, 2018.

[24] E. D. Fernández-Nieto, M. Parisot, Y. Penel, and J. Sainte-Marie. A hierarchy of dispersive layer-averaged approximations of Euler equations for free surface flows. *Communications in Mathematical Sciences*, 16(5):1169–1202, 2018.

[25] E.D. Fernández-Nieto, D. Bresch, and J. Monnier. A consistent intermediate wave speed for a well-balanced HLLC solver. *Comptes Rendus Mathematique*, 346(13-14):795–800, jul 2008.

[26] J. M. N. T. Gray and A. N. Edwards. A depth-averaged μ(I)-rheology for shallow granular free-surface flows. *Journal of Fluid Mechanics*, 755:503–534, 2014.

[27] I. R. Ionescu, A. Mangeney, F. Bouchut, and R. Roche. Viscoplastic modeling of granular column collapse with pressure-dependent rheology. *Journal of Non-Newtonian Fluid Mechanics*, 219(0):1–18, 2015.

[28] R. M. Iverson and D. L. George. A depth-averaged debris-flow model that includes the effects of evolving dilatancy. I. Physical basis. *Proceedings of the Royal Society A: Mathematical, Physical and Engineering Sciences*, 470(2170):20130819, 2014.

[29] R. M. Iverson, M. Logan, and R. P. Denlinger. Granular avalanches across irregular three-dimensional terrain: 2. Experimental tests. *Journal of Geophysical Research: Earth Surface*, 109(F1), mar 2004.

[30] R. Jackson. *The Dynamics of Fluidized Particles*. Cambridges Monographs on Mechanics. Cambridge University Press, 2000.

[31] P. Jop, Y. Forterre, and O. Pouliquen. A constitutive law for dense granular flows. *Nature*, 441(7094):727–730, 2006.

[32] P. Jop, Y. Forterre, and O. Pouliquen. Initiation of granular surface flows in a narrow channel. *Physics of Fluids (1994-present)*, 19(8):088102, 2007.

[33] K. Kelfoun and T. H. Druitt. Numerical modeling of the emplacement of Socompa rock avalanche, Chile. *Journal of Geophysical Research*, 110(B12), 2005.

[34] P.-Y. Lagrée, L. Staron, and S. Popinet. The granular column collapse as a continuum: validity of a two-dimensional Navier-Stokes with a μ(I)-rheology. *Journal of Fluid Mechanics*, 686:378–408, 2011.

[35] A. Lucas, A. Mangeney, and J. P. Ampuero. Frictional velocity-weakening in landslides on Earth and on other planetary bodies. *Nature Communications*, 5(1), mar 2014.

[36] A. Mangeney, F. Bouchut, N. Thomas, J. P. Vilotte, and M. O. Bristeau. Numerical modeling of self-channeling granular flows and of their levee-channel deposits. *Journal of Geophysical Research: Earth Surface*, 112(F2):n/a–n/a, 2007. F02017.

[37] A. Mangeney, O. Roche, O. Hungr, N. Mangold, G. Faccanoni, and A. Lucas. Erosion and mobility in granular collapse over sloping beds. *Journal of Geophysical Research: Earth Surface (2003–2012)*, 115(F3), 2010.

[38] A. Mangeney-Castelnau, F. Bouchut, J. P. Vilotte, E. Lajeunesse, A. Aubertin, and M. Pirulli. On the use of Saint Venant equations to simulate the spreading of a granular mass. *Journal of Geophysical Research: Solid Earth*, 110(B9):n/a–n/a, 2005. B09103.

[39] A. Mangeney-Castelnau, J.-P. Vilotte, M. O. Bristeau, B. Perthame, F. Bouchut, C. Simeoni, and S. Yerneni. Numerical modeling of avalanches based on Saint Venant equations using a kinetic scheme. *Journal of Geophysical Research: Solid Earth*, 108(B11):2527–2544, 2003.

[40] N. Martin, I. R. Ionescu, A. Mangeney, F. Bouchut, and M. Farin. Continuum viscoplastic simulation of a granular column collapse on large slopes: μ(I) rheology and lateral wall effects. *Physics of Fluids*, 29(1):013301, 2017.

[41] C. Parés. Numerical methods for nonconservative hyperbolic systems: a theoretical framework. *SIAM Journal on Numerical Analysis*, 44(1):300–321, 2006.

[42] M. Peruzzetto, J.-C. Komorowski, A. Le Friant, M. Rosas-Carbajal, A. Mangeney, and Y. Legendre. Modeling of partial dome collapse of La Soufrière of Guadeloupe volcano: implications for hazard assessment and monitoring. *Scientific Reports*, 9(1), sep 2019.

[43] M. Peruzzetto, A. Mangeney, F. Bouchut, G. Grandjean, C. Levy, Y. Thiery, and A. Lucas. Topography curvature effects in thin-layer models for gravity-driven flows without bed erosion. working paper or preprint, December 2020.

[44] M. Peruzzetto, A. Mangeney, G. Grandjean, C. Levy, Y. Thiery, J. Rohmer, and A. Lucas. Operational Estimation of Landslide Runout: Comparison of Empirical and Numerical Methods. *Geosciences*, 10(11):424, oct 2020.

[45] M. Pirulli and A. Mangeney. Results of Back-Analysis of the Propagation of Rock Avalanches as a Function of the Assumed Rheology. *Rock Mechanics and Rock Engineering*, 41(1):59–84, 2008.

[46] E.B. Pitman and L. Le. A two-fluid model for avalanche and debris flows. *Philosophical Transactions of the Royal Society of London A: Mathematical, Physical and Engineering Sciences*, 363(1832):1573–1601, 2005.

[47] O. Pouliquen. On the shape of granular fronts down rough inclined planes. *Physics of Fluids*, 11(7):1956–1958, 1999.

[48] O. Pouliquen. Scaling laws in granular flows down rough inclined planes. *Physics of Fluids (1994-present)*, 11(3):542–548, 1999.

[49] O. Pouliquen and Y. Forterre. Friction law for dense granular flows: application to the motion of a mass down a rough inclined plane. *Journal of Fluid Mechanics*, 453:133–151, 2002.

[50] O. Pouliquen and Y. Forterre. A non-local rheology for dense granular flows. *Philosophical Transactions of the Royal Society A: Mathematical, Physical and Engineering Sciences*, 367(1909):5091–5107, dec 2009.

[51] S. B. Savage and K. Hutter. The motion of a finite mass of granular material down a rough incline. *Journal of Fluid Mechanics*, 199:177–215, 1989.

[52] L. Staron, P.-Y. Lagrée, and S. Popinet. The granular silo as a continuum plastic flow: The hour-glass vs the clepsydra. *Physics of Fluids (1994-present)*, 24(10), 2012.

[53] G. Stelling and M. Zijlema. An accurate and efficient finite-difference algorithm for non-hydrostatic free-surface flow with application to wave propagation. *International Journal for Numerical Methods in Fluids*, 43(1):1–23, 2003.

[54] Y. Yamazaki, Z. Kowalik, and K.F. Cheung. Depth-integrated, non-hydrostatic model for wave breaking and run-up. *Numerical Methods in Fluids*, 61:473–497, 2008.